Parameters for sensing lipid loosening at the inner nuclear membrane by amphipathic helices

Shoken Lee[1], Anabel-Lise Le Roux[2], Mira Mors[3], Stefano Vanni[3, 4], Pere Roca-Cusachs[2, 5] and Shirin Bahmanyar[1,*]

[1] Department of Molecular Cellular and Developmental Biology, Yale University, 260 Whitney Ave, Yale Science Building 116, New Haven, CT 06511, USA

[2] Institute for Bioengineering of Catalonia, the Barcelona Institute of Technology (BIST), Barcelona, Spain

[3] Department of Biology, University of Fribourg, Switzerland

[4] Swiss National Center for Competence in Research Bio-Inspired Materials, University of Fribourg, Fribourg CH-1700, Switzerland

5 Departament de Biomedicina, Unitat de Biofísica i Bioenginyeria, Facultat de Medicina i Ciències de la Salut, Universitat de Barcelona, Barcelona, Spain

*Correspondence: shirin.bahmanyar@yale.edu

Summary

Amphipathic helices (AHs) detect differences in bulk membrane properties, but how AHs detect the nuclear membrane surrounding the genome is not well understood. Here, we computationally screened for candidate AHs in a curated list of characterized and putative human inner nuclear membrane (INM) proteins. Cell biological and *in vitro* experimental assays combined with computational calculations demonstrate that AHs detect lipid packing defects over electrostatics to bind to the INM, indicating that the INM is loosely packed under basal conditions. Membrane tension resulting from hypotonic shock further promoted AH binding to the INM, whereas cell-substrate stretch did not recruit membrane tension-sensitive AHs. Thus, distinct mechanical inputs enhance lipid loosening at the INM to different degrees, which AHs in INM proteins may harness for downstream biochemical functions. Our resource provides a framework for future studies on the contributions of lipid-protein interactions at the INM and enables exploration of the membrane properties of the INM under different conditions.

Introduction

Membrane-bound organelles have characteristic biophysical properties driven by their distinct lipid compositions. The endoplasmic reticulum (ER) and Golgi apparatus are defined by loose lipid packing and low electrostatics, whereas organelles of the late secretory pathway, plasma membrane, and mitochondria generally contain more tightly packed lipids and are rich with negatively charged lipids (Bigay and Antonny, 2012; Ernst et al., 2016; Holthuis and Menon, 2014). Protein regions called amphipathic helices (AHs) recognize these differences in bulk membrane properties and insert in the polar-apolar region of a single leaflet of a lipid bilayer (Drin and Antonny, 2010; Giménez-Andrés et al., 2018). The composition of the hydrophilic and hydrophobic amino acid residues that make up each face of the helix determines whether an AH detects membrane electrostatics or loose lipid packing (Drin et al., 2007; Hofbauer et al., 2018; Pranke et al., 2011) – this mechanism is distinct from the recognition of specific lipid species based on the head group composition (Lemmon, 2008). Loose lipid packing results from an increased level of unsaturated fatty acids or cone-shaped lipids, which induces lipid packing defects – regions in which hydrophobic tails are exposed to the aqueous cytoplasm (Bigay and Antonny, 2012; Holthuis and Menon, 2014). AHs with few charged amino acids on their hydrophilic face bind membranes through the highly sensitive detection of membrane packing defects driven by hydrophobic interactions (Drin et al., 2007; Pranke et al., 2011; Vanni et al., 2014). Some AHs (e.g., Amphipathic lipid-packing sensors (ALPS) motifs) with no to very few charged amino acids are exquisite sensors of membrane curvature, the geometry of which intrinsically contains a high density of packing defects (Drin et al., 2007; Pranke et al., 2011; Vanni et al., 2014).

While a lot is known about how AHs detect differences in bulk membrane properties, little is known about whether these detection modes are relevant to the nuclear envelope (NE). The NE is unique among organelles because it is a relatively flat, uniform membrane sheet, with the exception of curved membranes at fusion points between the inner and outer nuclear membrane that are highly occupied by nuclear pore complex proteins (Bahmanyar and Schlieker, 2020; Cornell and Antonny, 2018). In addition, the NE shares a single membrane with the ER, which makes isolating the NE biochemically challenging and hinders the

direct determination of its lipid composition. The recent development of fluorescent INM lipid biosensors bypassed this challenge and indicated that the NE across multiple organisms contains the cone-shaped lipid diacylglycerol (DAG) (Foo et al., 2023; Lee et al., 2023; Romanauska and Köhler, 2018). Thus, the nuclear membrane may be loosely packed like the ER despite its flat structure. A lipid biosensor for phosphatidylserine (PS) suggested that the surface of the INM may also be defined by electrostatics (Niu et al., 2024). The degree to which negative charge versus packing defects define the membrane properties of the NE remains an important issue to resolve.

Amphipathic helices are found in many nucleoporins, which is in line with the high curved feature of the nuclear pore membrane (Amm et al., 2023; Hamed and Antonin, 2021; Kralt et al., 2022). Less is known about how AHs detect and bind to the relatively flat surface of the INM. The best-known example of AH detection of the INM at the non-NPC regions is by the soluble, rate-limiting enzyme in phosphocholine synthesis, CCTa/PCYT1A (Cornell and Antonny, 2018; Cornell, 2016; Haider et al., 2018). More recently, the resident INM nucleocytoskeletal protein Sun2 was also shown to contain an AH with a preference for packing defects (Lee et al., 2023). These examples of INM association by AHs suggest that the detection of bulk INM properties may be a more pervasive mechanism linked to NE-dependent processes.

Defining bulk INM properties and how they are sensed is particularly important when it comes to mechanical forces imposed on the NE. Forces induced by cell-substrate interactions are transmitted to cytoskeletal forces imposed directly on the NE, which have profound downstream effects on gene expression profiles and cell fate (Carley et al., 2021; Kalukula et al., 2022; Miroshnikova and Wickström, 2022; Nava et al., 2020). Recently, NE tension resulting from hypotonic shock due to cell injury or from physical confinement was shown to promote association of the C2 domain of the enzyme cPLA2 with the INM (Enyedi et al., 2016; Lomakin et al., 2020; Venturini et al., 2020). It has been proposed that cPLA2 recognizes increased packing defects at the INM; however, the extent to which different mechanical inputs affect lipid order at the INM beyond this example remains unexplored.

Here, we systematically identify lipid-sensing AH regions in putative and known transmembrane-containing NE-associated proteins. We define determinants in AHs that facilitate binding to the INM and use multidisciplinary approaches to demonstrate that they preferentially associate with membrane packing defects. We utilize the property of AHs as exquisite detectors of lipid packing defects to determine the extent of INM lipid loosening in response to distinct mechanical inputs. Our findings provide a framework for understanding how forces impact the membrane properties of the NE and a resource for future studies on the contributions of lipid-protein interactions to NE-dependent functions.

Results

For an understanding of the amino acid-sequence code used by AHs to detect the flat membrane territory of the NE, we took a systematic approach to identify and characterize putative AH regions in a large number of proteins shown to associate with the NE. Our prior search used machine-learning-based algorithms to yield 7 predicted AHs in characterized inner nuclear membrane proteins, including the LEM-domain family and LINC complex proteins, as well as Lamin B Receptor and NEMP1(Lee et al., 2023). To generate a more comprehensive list of known and previously uncharacterized nuclear membrane-associated proteins, we compiled data from biochemical studies in which the NE proteome was determined in distinct tissue types (Cheng et al., 2019; Korfali et al., 2010; Korfali et al., 2012; Schirmer et al., 2003; Wilkie et al., 2011) and obtained a list of 410 proteins (Fig. 1A; see Fig. S1A and S1B and Methods for methodological details and Tables S1-S5 for the complete lists of the proteins). We refined this list to 281 proteins by prioritizing those in which more than one publication supported NE association or those with additional support for NE association from the Human Protein Atlas and UniProt (Fig. S1A and Methods; see Tables S6-S7 for the complete lists of proteins). We leveraged a previously published in-silico prediction of AHs developed by a deep-learning-based algorithm called MemBrain (Feng et al., 2022) to identify potential AHs within our extensive list of compiled proteins. Their published predictions covered 11,750 putative transmembrane proteins from various organisms, hereafter referred to as the "MemBrain list." We used a custom Python script with the UniProt Application Programming Interface (API) to filter

the MemBrain list down to only putative transmembrane proteins from humans (Fig. S1A and Tables S7-S8). Merging the compiled list of nuclear membrane proteins with the filtered MemBrain analysis resulted in 87 proteins that contained either one or two predicted AHs (Fig. 1; Fig. S1A; Tables S9-S10). Similar to our prior analyses of AHs in characterized NE proteins (Lee et al., 2023), AHs were identified from the 'MemBrain' list in Sun2, Sun1, NEMP1, LEMD2, and Man1 (Fig. S1C). We eliminated potential false positives with further analysis of AH amino acid sequences identified through 'MemBrain' by using AlphaFold2 (Jumper et al., 2021) to confirm that these regions are predicted helices, TMHMM (Krogh et al., 2001) to eliminate regions predicted as transmembrane regions, and HeliQuest (Gautier et al., 2008) to confirm their strong amphiphilicity. Our final list included 46 proteins with 61 promising AH candidates (Fig. 1A and Table S11).

We next tested whether our list of putative AHs associate with cytosolic membrane-bound organelles that have well-defined lipid territories. We reasoned that an understanding of whether AHs from NE-associated proteins bind different lipid territories of cytosolic membrane organelles will inform our understanding of the composition of the nuclear membrane. We successfully cloned 58 AH candidates appended to mNeonGreen (mNG) fluorescent protein at their C-terminus and determined their localizations when expressed in living U2OS cells. Twenty-three AHs localized to the cytosol and nucleoplasm, similar to mNG alone (Fig. S2), and this was not because the mNG was abnormally cleaved from the AH sequence (Fig. S3). The 35 AHs that localized to membranes displayed varied localization patterns that resembled mitochondria, ER, Golgi and one AH localized to the cell periphery resembling the plasma membrane (Fig. 1B; Figs. S4-S6; Table S12). Note that although the AH-mNG proteins are small enough to diffuse into the nucleus, none of the AHs are exclusively localized to the INM. This is in line with prior work demonstrating that full-length proteins direct the organellar localization of AHs, whereas expressing AHs on their own reveals their independent membrane composition binding preferences (Doucet et al., 2015; Lee et al., 2023; Pranke et al., 2011; Prévost et al., 2018). Note that a limitation of this approach is that an N-terminal AH could potentially serve as a mitochondrial import signal (Abe et al., 2000).

We determined if there was a pattern in the amino acid sequences that could suggest an adaptation to different lipid territories and how this might relate to the ability of AHs to associate with the INM when directed to the nucleus. There were no differences in length, net charge, or hydrophobic moment that clearly discriminated AHs (Fig. 2A-2C). We also compared the "D factor" for AH sequences, which serves as a prediction tool for the likelihood of association to lipid bilayers through a combined hydrophobic moment and net charge calculation (possible association if D > 0.65 and likely association if D > 1.3) (Gautier et al., 2008), but did not find any major differences between the different groupings (Fig. 2D).

A trend was revealed from analysis of the amino acid compositions of the hydrophilic and hydrophobic faces of 32 AHs (Fig. 2E and 2F; Fig. S7) in which ER, Golgi or plasma membrane ('non-mitochondrial')-localized AHs were enriched in Ser/Thr residues in the hydrophilic face (Fig. 2F) and enriched in Leu residue relative to Ile/Phe/Trp residues in the hydrophobic face (Fig. S7). Ser/Thr residues in the hydrophilic face of AHs in place of other charged residues, such as Arg/Lys suggests that the driving force for membrane binding is through the hydrophobic effect rather than electrostatic charges (Bigay and Antonny, 2012). This is exemplified in the ALPS motifs of ArfGAP1 and GMAP210 that contain few Arg/Lys residues in the hydrophilic faces – the prerequisite for membrane binding for ALPS motifs is lipid packing defects, making them exquisite sensors of membrane curvature (Drin et al., 2007; Pranke et al., 2011; Vanni et al., 2014; Vanni et al., 2013). Indeed, Golgi and ER-localized AHs contained a higher ratio of Ser/Thr residues to Arg/Lys residues in the hydrophilic face, indicating a preference for membrane territories with lipid packing defects (Fig. 2G).

Directing ten of the AH-mNG constructs to the nucleus by appending a nuclear localization signal (NLS) to the C-terminus revealed greater INM localization for AHs that localize to the Golgi, ER or plasma membrane when expressed in the cytosol (Fig. 3A-3C). This was in contrast to the lack of INM localization of AH-mNG constructs appended to an NLS that localize to mitochondria when expressed in the cytosol – when directed to the nucleus, these localized to the nucleoplasm and nuclear bodies in a manner that resembled the distribution of the mNG-NLS control (Fig. 3B-3D). These results suggest that electrostatics alone is insufficient to promote INM binding because 'mitochondrial' AH-mNG constructs contain low

S/T:R/K ratios in their hydrophilic face (Fig. 2F and 2G). Interestingly, the ALPS motif of Nup133 (Drin et al., 2007; Nordeen et al., 2020) that has a high S/T:R/K ratio as well as the ALPS motifs of ArfGAP1 (Bigay et al., 2005; Mesmin et al., 2007) that also has few charged residues were less associated with the INM relative to the AH of Nup153 (Vollmer et al., 2015) and the other INM-associated AHs tested (Fig. 3; Fig. S8). Thus, a combination of electrostatics and membrane packing defects is likely be required for robust AH association with the INM under basal conditions.

We directly tested the role that electrostatics and lipid packing defects play in promoting AH binding to the INM by increasing the S/T:R/K ratio in a non-INM localized AH. Mutating R/K amino acids in the hydrophilic face of the AH of TMEM126 to S/T residues incrementally increased its INM association in cells (Fig. 4A). Wild-type and K11S/R15S mutated AH peptides tagged with monomeric GFP were purified from bacterial cells (Fig. S9) and their interactions with giant unilamellar vesicles (GUVs), which have very low intrinsic local curvature similar to the INM, composed of different lipid compositions were analyzed. We prepared fluorescently-labeled GUVs with lipid compositions that represent low packing defects (dioleoyl-phosphatidylcholine (DOPC) ('PC-alone')); a highly charged lipid bilayer (10% dioleoyl-phosphatidylserine (DOPS) ('+PS') or 10% dioleoyl-phosphatidylinositol (DOPI) ('+PI')); and a lipid bilayer with packing defects (10% dioleoyl-glycerol (DOG) ('+DAG') (Vamparys et al., 2013; Vanni et al., 2014) or saturated, methyl-branched chains phospholipid: 10-100 % diphytanoyl-phosphatidylcholine ('+Branched PC') (Čopič et al., 2018; Garten et al., 2015)). Neither the wild-type nor the K11S/R15S mutant AH bound to PC-alone GUVs, while both the wild-type and mutant AH bound to the +PS or +PI GUVs, with the wild-type displaying greater association (Fig. 4B). These results are in line with electrostatics playing a role in membrane association through the positively charged amino acids in the hydrophilic face of both constructs (Drin et al., 2007; Pranke et al., 2011). Hydrophobic driving forces overcame the need for electrostatics only for K11S/R15S mutated AH peptides, which robustly associated with GUVs containing either the cone-shaped lipid DAG or branched PC known to induce packing defects (Čopič et al., 2018; Garten et al., 2015; Vamparys et al., 2013; Vanni et al., 2014). The fact that only the K11S/R15S mutant, and not the wild-type AH, bound to GUVs containing packing defects (Fig. 4C)

suggests that a higher S/T:R/K ratio in the hydrophilic face of the AH of TMEM126 promoted membrane binding when nuclear-localized because the INM contains packing defects.

We used a computational predictor based on molecular dynamics simulations to further support the idea that the presence of packing defects contributes to the driving force for INM-association of AHs. This predictor, called PMIpred, calculates the difference in free energy reduction upon AH helix association to 'stretched' and 'non-stretched' membranes bilayers containing a constant number of lipids (ΔΔF) (Fig. 5A) (van Hilten et al., 2023; van Hilten et al., 2022; van Hilten et al., 2024). 'Stretched' membranes are in principle under tension - an increased area occupied per lipid and lipid distortion expose acyl chains, which is equivalent to the definition of packing defects (Pinot et al., 2018; van Hilten et al., 2020). When the binding of an AH to a 'stretched' membrane is calculated to have a greater difference in free energy reduction than when bound to an 'unstretched' membrane, hydrophobicity is a driving force for membrane association. These AHs would be predicted to be highly sensitive to packing defects. We compared the ΔΔF for our AH candidates (58 in total tested by live imaging (Fig. 1)) to those of characterized AHs (van Hilten et al., 2023), which fall into three categories defined by their sensitivity to packing defects: binders (any membrane independent of curvature-induced packing defect), sensors (only bind curved membranes) and non-binders (don't bind membranes) (van Hilten et al., 2023). We found that the AHs in our list that localized to cytosolic organelle membranes (35 in total) tended to have higher absolute values of ΔΔF than those that were cytosolic and were within a similar range as benchmarked AHs characterized as membrane binders and sensors (Fig. 5B, left). The AHs in our list with greater association to the INM had larger absolute values of ΔΔF than those with weak to no association, further supporting our findings that INM binding relies on detecting packing defects (Fig. 5B, right).

Taken together, we conclude that the lipid composition of the INM has adapted to its relatively flat membrane structure by containing lipids that induce packing defects, which can be harnessed by AH sequences in which hydrophobicity is the driving force for peripheral membrane association.

We reasoned that because of the lack of curved membranes in the flat yet unpacked membrane territory of the INM, AH binding may be exquisitely sensitive to effects on the density of lipid packing

defects resulting from membrane tension. The highly characterized AH of the ALPS motif from ArfGAP1 that is highly sensitive to membrane packing defects (Pinot et al., 2018; Shen et al., 2022), as well as a subset of AHs of NE-associated proteins, were recruited to the nuclear rim upon hypotonic shock (Fig. 6A and 6B; Fig. S10). The greater response to hypotonic shock observed for the K11S/R15S mutant of AH(TMEM126A) compared to the wild-type AH is in line with the idea that INM association and membrane tension sensing share detection of packing defects as the underlying mechanism (Fig. 6C; Fig. S10). Together, these results suggest that membrane tension-sensing is highly prevalent across AHs in NE proteins that are characterized by a paucity of charged residues in the hydrophilic face – for these AHs, the driving force for membrane binding is hydrophobic interactions suggesting that membrane tension upon hypotonic shock results in lipid loosening sufficient to expose hydrophobic acyl chains.

The ability to use AHs as INM tension sensors led us to test whether AHs can sense any changes in INM lipid packing that may occur in response to cytoskeletal forces imposed on the NE. We used a custom membrane stretch device to impose equibiaxial stretch on living HeLa cells (Kosmalska et al., 2015). The maximal cell stretch that could be applied without rupturing the plasma membrane caused the nucleus to deform (see fold increase of cross-sectional nucleus area and pseudo-colored image overlay in Fig. 6D), which is known to occur under this regime through nucleo-cytoskeletal interactions (Lombardi et al., 2011), yet this did not induce sufficient membrane tension to promote AH binding (Fig. 6D). Thus, we conclude that local forces produced from the cytoskeleton do not induce lipid packing defects to the same extent as hypotonic shock. We suggest that these forces should be treated as highly distinct in their effects on the nuclear membrane, highlighting the importance of determining the impact on nuclear membrane lipids under specific inputs that lead to downstream nuclear and cellular responses.

Discussion

In the current study, we offer a resource of a curated and comprehensive list of characterized and uncharacterized transmembrane-containing NE proteins and further analyzed whether they contain predicted AHs. We validated that AHs from NE-associated proteins localize to membrane-bound organelles

when expressed in the cytosol and characterized their INM binding propensities. The curated list includes proteins with AHs that are mutated in diseases associated with the NE (e.g., TMEM214) (Meinke et al., 2020; Reicher et al., 2024; Wilkie et al., 2011), an E3 ligase (e.g., RNF170) (Lu et al., 2011; Song et al., 2020; Wright et al., 2015), and many uncharacterized NE-associated proteins (e.g., TMEM260). By analogy to other membrane-associated AHs in transmembrane proteins, these AHs may regulate the activity or stability (Chua et al., 2017; Halbleib et al., 2017; Kefauver et al., 2020; Lee et al., 2023) or engage in membrane deformation in the context of the full-length protein (Amm et al., 2023; Brady et al., 2015; Breeze et al., 2016; Kayagaki et al., 2021; Kralt et al., 2022). Our study of AHs in relation to the NE further suggests that AHs can serve as sensors of membrane tension, which may be highly relevant to mechanisms involving mechanosensing and mechanotransduction at the NE.

Inner nuclear membrane-association of the ALPS motif of ArfGAP1, which was shown to be sensitive to membrane tension *in vitro* and *in silico* (Pinot et al., 2018; Shen et al., 2022), and AHs of INM proteins in response to hypotonic shock suggests that these AHs are sensitive to lipid loosening resulting from membrane tension (Pinot et al., 2018; van Hilten et al., 2020). The fact that tension-sensitive AHs did not bind to the INM upon equibiaxial cellular stretch indicates that the extent of lipid loosening and the induction of packing defects depends on the type of mechanical input imposed on the NE. It is established that nuclear deformation upon cellular stretch affects nucleocytoplasmic transport by mechanical modulation of NPCs (Andreu et al., 2022; Elosegui-Artola et al., 2017). Thus, in contrast to hypotonic shock, in which membrane tension is induced by internal forces uniformly imposed on the INM, external cytoskeletal forces on the nucleus induced by cellular stretch may only impose membrane tension locally. These external forces may further be dissipated through tension on NPCs and the nuclear lamina (Carley et al., 2021; Taniguchi et al., 2024) to give rise to a distinct mechanical response.

Our in-depth analysis of AHs in NE-associated proteins suggests that the INM contains packing defects, even under basal conditions. This membrane property may help accommodate nuclear membrane remodeling and repair (Bahmanyar and Schlieker, 2020; Penfield et al., 2020). Additionally, the lipid content of the NE can be altered by both local and global lipid metabolism (Barbosa et al., 2019; Haider et

al., 2018; Lee et al., 2023; Romanauska and Köhler, 2018; Romanauska and Köhler, 2021; Samardak et al., 2024; Sołtysik et al., 2021; Tsuji et al., 2019), which has downstream consequences, including local protein degradation (Lee et al., 2023), nuclear growth (Foo et al., 2023; Mauro et al., 2022), and changes in nuclear fragility (Baird et al., 2023; Romanauska and Köhler, 2023).

Our study focuses on lipid packing defect detection by AHs, but our identification of AHs in INM proteins with charged amino acid residues on the hydrophilic face, although correlative, fits with the possibility that low electrostatics are likely present at the INM. However, these AHs did not bind the INM of U2OS cells under basal conditions, suggesting that lipids with negatively charged headgroups may be more enriched in specific cell types or regulated under certain conditions. Indeed, PA is present at the INM in fungi under specific circumstances and, interestingly, is detected by the AH of the membrane remodeling protein Chmp7 (Garcia et al., 2022; Romanauska and Köhler, 2018; Thaller et al., 2021). Some mammalian cell types can contain PS at the INM; thus, there is more to learn about the role of electrostatics at the INM (Niu et al., 2024; Tsuji et al., 2019). Our work sets the stage for understanding mechanisms involving AHs in INM proteins in detecting changes in lipid composition, with broad implications in how the biophysical properties of the INM control NE-dependent functions in both healthy conditions and in diseases associated with the NE.

Acknowledgments

We thank J.M. Gendron (Yale University, New Haven, CT, USA), Zhouyang Shen and Philipp Niethammer (Memorial Sloan Kettering Cancer Center, New York, NY, USA), Taki Nishimura (Osaka University, Osaka, Japan) and Takaho Tsuchiya (Tsukuba University, Ibaraki, Japan) for technical advice; Dorus Gadella (University of Amsterdam, Amsterdam, the Netherlands), Michael Davidson (Florida State University, Tallahassee, FL, USA) and Philipp Niethammer for reagents. We thank F. Moore (Yale University, New Haven, CT, USA) for comments on the manuscript. We thank Yale Nucleus Club and BMB Club for helpful discussions. This work was supported by: NIH R01 (GM131004) to S.B.; Swiss National Science Foundation (grant CRSII5_189996), and the European Research Council under the

European Union's Horizon 2020 research and innovation program (grant agreement no. 803952) to S.V.; The Spanish Ministry of Science and Innovation (PID2022-142672NB-I00), the European Research Council (grant 101097753 MechanoSynth), the Generalitat de Catalunya (2017-SGR-1602), the prize "ICREA Academia" for excellence in research to P.R.C. IBEC is a recipient of a Severo Ochoa Award of Excellence from MINCIN.

Author contributions

S. Lee and S. Bahmanyar conceived the project. S. Lee performed most of the experiments and data analysis. A.L. Le Roux and P. Roca-Cusachs conceived experiments on cellular stretch and interpreted data. A.L. Le Roux performed cellular stretch experiments. M. Mors performed ΔΔF analysis and was supervised by S. Vanni. S. Lee and S. Bahmanyar wrote the manuscript with input from other authors. S. Bahmanyar supervised the project.

Declaration of Interests

The authors declare no competing interests.

Lead Contact

Requests for further information, resources, and reagents should be directed to Shirin Bahmanyar (shirin.bahmanyar@yale.edu).

Materials Availability

Materials generated in this study are available upon request to the Lead Contact.

Data and Code Availability

Raw data generated in this study are available upon request to the Lead Contact. Python scripts are found at GitHub as mentioned in Materials and Methods.

Materials and Methods

Reagents and resources

REAGENT or RESOURCE	SOURCE	IDENTIFIER
Antibodies		
Mouse anti-mNeonGreen	ChromoTek	Cat# 32f6-100, RRID:AB_2827566
Mouse anti-tubulin alpha	Millipore	Cat# 05-829, RRID:AB_310035
Bacterial and virus strains		
Escherichia coli BL21(DE3) cells	New England Biolabs	Cat# C2527
Chemicals, peptides, and recombinant proteins		
18:1 (Δ9-Cis) PC (DOPC)	Avanti	Cat# 850375C
18:1 DG (DAG)	Avanti	Cat# 800811C
18:1 PS (DOPS)	Avanti	Cat# 840035C
18:1 PI (DOPI)	Avanti	Cat# 850149P
4ME 16:0 PC (DPhPC)	Avanti	Cat# 850356C
Experimental models: Cell lines		
U2OS	Slack lab (Harvard Medical School)	N/A
HeLa	Single Molecule Biophotonics group at ICFO (The Institute of Photonic Sciences)	N/A
Recombinant DNA		
AH candidates-mNG	This study	N/A
AH candidates-mNG-NLS	This study	N/A
mNG-NLS without an AH	Ref(Lee et al., 2023)	N/A
mNG alone (pmNG-N3)	This study	N/A
DsRed-KDEL	Bewersdorf lab (Yale School of Medicine)	N/A
mScaret-Giantin	Dorus Gadella(Bindels et al., 2017)	Addgene plasmid # 85049; RRID:Addgene_85049

mRuby-Mito	Michael Davidson	Addgene plasmid # 55874; RRID:Addgene_55874
AH(Nup133)-mNG	This study	N/A
AH(Nup133)-mNG-NLS	This study	N/A
AH(Nup153)-mNG	This study	N/A
AH(Nup153)-mNG-NLS	This study	N/A
ALPS1-ALPS2(ArfGAP1)-mNG-NLS	This study	N/A
6xHis-SUMO-AH(TMEM126A) WT-AcGFP1	This study	N/A
6xHis-SUMO-AH(TMEM126A) K11S/R15S-AcGFP1	This study	N/A
Software and algorithms		
FIJI	Ref(Schindelin et al., 2012)	https://imagej.net/Fiji
GraphPad Prism 9	GraphPad Software	https://www.graphpad.com/scientificsoftware/prism/
SnapGene	GSL Biotech LLC	https://www.snapgene.com/
TMHMM	Ref(Krogh et al., 2001)	https://services.healthtech.dtu.dk/service.php?TMHMM-2.0
HeliQuest	Ref(Gautier et al., 2008)	https://heliquest.ipmc.cnrs.fr/
Python version 3.8 or 3.11	Python Software Foundation	https://www.python.org/
Anaconda	Anaconda Inc	https://www.anaconda.com/products/distribution

Computational screening

Listing established/putative nuclear envelope proteins

The following process was performed by custom Python scripts found on Github (https://github.com/shokenlee/Nuclear_proteome). To list NE proteins, we merged the published dataset of NE proteomics from 5 papers (Cheng et al., 2019; Korfali et al., 2010; Korfali et al., 2012; Schirmer et al., 2003; Wilkie et al., 2011) using the UniProtID of the human protein as the unique identifier. First, we first obtained the UniProtID for each protein if it was not available in the original dataset. Specifically, either NCBI accession numbers in the dataset of (Schirmer et al., 2003) or gene names in the dataset of (Korfali et al., 2010; Korfali et al., 2012)(Wilkie et al., 2011) were converted to UniProt ID using Retrieve/ID mapping or API of UniProt, respectively. Some obsolete or invalid gene records were automatically eliminated during this process. The dataset in (Cheng et al., 2019) already contained UniProt ID. Next, for proteins in the original dataset that were not from humans but from mice or rats, we retrieved their human orthologues from UniProt using the gene name in humans via API (e.g., the human orthologue of the mouse Ctdnep1 is found by querying "gene name: ctdnep1 & organism: Homo sapiens"). This method leveraged the fact that human, mouse, and rat genes have the same names in orthologues in most cases. Although this method was not as stringent as a sequence-based orthologue search, we found no instances of retrieving a false orthologue in the final list of AH candidates. Finally, the five NE proteome datasets were merged. We are aware that (Cheng et al., 2023) published another dataset of their NE proteomics, but this was not included because we had already completed our AH screening and listed candidates when it was published.

Human Protein Atlas data (Table S6 in ref(Thul et al., 2017)) were screened to obtain a list of nuclear proteins based on: 1) “IF location score” contains any word including “nucle” (e.g. ‘nuclear membrane’, ‘nucleoli’); 2) “Reliability” being either “Supported” or “Validated.”

UniProt subcellular location data were obtained for the 410 NE proteins through the API. Each protein was considered a NE/ER protein if all of three criteria were met: 1) Subcellular location information contained any of the following ['Nucleus outer membrane', 'Nucleus membrane', 'Nucleus inner membrane', 'Nucleus, nuclear pore complex', 'Nucleus envelope', 'Nucleus lamina', 'Endoplasmic reticulum membrane',

'Endoplasmic reticulum', 'Sarcoplasmic reticulum membrane', 'Endoplasmic reticulum-Golgi intermediate compartment membrane', 'Endoplasmic reticulum lumen']; 2) The evidence was manually, but not automatically-curated, information. Specifically, the evidence code was any of the following: ['ECO:0000269' (experimental evidence), 'ECO:0000305' (inference from paper), 'ECO:0000250' (seq similarity), 'ECO:0000255' (seq model), 'ECO:0000312' (imported from other database), 'ECO:0007744' (a combination of experimental and computational evidence)]; 3) The evidence was not solely reliant on any of the 5 NE proteome papers (PMIDs: ['12958361', '20693407', '20876400', '22990521', '31142202']).

Finally, the NE protein list with UniProt subcellular location data was merged with the Human Protein Atlas list using UniProtID as the unique identifier. Each protein was considered a NE protein if 1) it appeared in 2 or more NE proteome paper, or, 2) it appeared in only one NE proteome paper but was a nuclear protein in Human Protein Atlas or a NE/ER protein in UniProt.

Processing and merging MemBrain list with the NE protein list

The python scripts are found on Github (https://github.com/shokenlee/Find-AH-NE_MemBrain). The MemBrain prediction results for 11,759 proteins were downloaded from http://www.csbio.sjtu.edu.cn/bioinf/MemBrain/Download.htm. For each protein, the protein/gene names and organism name were obtained from UniProt through API. Then, the lineage information for each organism was obtained from UniProt through API and the protein list was screened for those from metazoan. Among them, attempts were made to map non-human proteins to human proteins by searching for the same name of the gene in humans, as conducted for the NE protein listing (see above). Finally, the MemBrain list was merged with the NE protein list using the UniProtID as the unique identifier.

Manual assessment of the AH candidates

The candidates of AH were further assessed manually based on: 1) distinctness of hydrophobic and hydrophilic faces with HeliQuest (Gautier et al., 2008); 2) secondary structure predicted by AlphaFold2 (Jumper et al., 2021); (3) possibility to be a transmembrane helix predicted by TMHMM (Krogh et al.,

2001). For (2), an AH candidate was removed if over the half of its length overlapped with a transmembrane domain. Note that a subset of partially transmembranous AHs was included in the final list because such AHs can be functionally important (Halbleib et al., 2017).

Plasmid construction

General note

Insertion of gene sequence was conducted by using In-Fusion HD Cloning Plus (638909; Takara) or Snap Assembly Master Mix (638948; Takara). Site-directed mutagenesis was performed by whole-plasmid PCR followed by circularization. Successful cloning was confirmed by sequencing for all constructs. A bipartite NLS from Xenopus laevis nucleoplasmin (KRPAATKKAGQAKKKK) (Lee et al., 2023) was used.

Candidates of AH tagged with mNG

The overall strategy for cost-effective construction of over 50 different AH-mNG constructs was to 1) synthesize DNA sequences as a small-scale pool, 2) amplify sequences by PCR with a common set of forward and reverse primers, 3) fuse the amplified sequences that have common overhang sequences on both ends into a linearized plasmid, which already encodes mNG on the C terminus. Consequently, AH-mNG constructs had the same linker sequence between AH and mNG, except varying number of glycine residues (see below). (1) A pool of single strand DNA encoding the sequences of the candidate AHs was synthesized by Twsit Biosciences. The sequence was AAACGGGCCCTCTAGAGCCACC*ATG*GGA (GGA)n XXX (GGT)n GGATCGAATTCTGCAGTCGACGGTAC, where XXX indicates each AH sequence, underlines indicate the anneal sites of the primers, *ATG* is the start codon, (GGA)n and (GGT)n are glycine linkers with 0 <= n <= 7. The length of the glycine linkers was chosen to keep the length variance of DNA sequences in the pool within +/- 10% of the median length for better efficiency of the oligo pool synthesis, as instructed by Twist Biosciences. (2) PCR was performed with the pooled oligo used as a template by the forward and reverse primers (noted above) with KAPA HiFi HotStart ReadyMix PCR Kit (50-196-5217; Roche Diagnostics) and purified with NucleoSpin Gel and PCR Clean-Up (740609;

Takara). (3) Purified amplicons were inserted into linearized plasmid with In-Fusion HD Cloning Plus (638909; Takara). The plasmid has a clipped CMV promoter(Morita et al., 2012) to minimize the expression level without compromising the transfection efficacy and mNG on the C terminus of the fusion site. The resulting plasmid has the glycine linker and an "NSAVDGTAGPGSAT" linker originated from the multi-cloning site of pEGFP-C2 in between AH and mNG. Approximately 120 colonies were picked and mini-prepped to obtain the 57 AH-mNG constructs.

mNG alone construct

The 'mNG alone' construct was generated by replacing EGFP in pEGFP-N3.

AH of Nup133, Nup153 and ArfGAP1 tagged with mNG

The ALPS-like motif (residues 245-263) of human Nup133 (UniProt ID Q8WUM0) was synthesized and PCR-amplified. The AH (residues 35-62) of human Nup153 (UniProt ID P49790) was amplified from pEGFP3-Nup153(Daigle et al., 2001). The AH (ALPS1-ALPS2) of ArfGAP1 was amplified from pGEX-6P-1-hs-ALPS 1-ALPS2-mCherry (a gift from Philipp Niethammer (Addgene plasmid # 187114; RRID: Addgene_187114)). The amplicon was inserted into the same backbone plasmid as the AH candidates to tag mNG with/without NLS.

His-SUMO-AH-AcGFP1

AcGFP1, which was shown to be monomeric in vitro(Gurskaya et al., 2003), was used. Firstly, AcGFP1 was amplified from GFP-Sec61b (a gift from Gia Voeltz) and inserted into pET-SUMO vector (ThermoFisher Cat# K30001). Then, the AH sequence was amplified from AH-mNG constructs and inserted in between SUMO and AcGFP1.

Cell culture

U2OS cells were grown at 37°C in 5% CO2 in DMEM low glucose (11885; Gibco) supplemented with 10% heat inactivated FBS (F4135) and 1% antibiotic-antimycotic (15240112; Gibco). HeLa cells were grown in DMEM (Thermo Fisher Scientific; 11960-044) supplemented with 10% FBS (Thermo Fisher Scientific; 10270-106), 1 mM sodium pyruvate (Thermo Fisher Scientific; 11360039) and 1% penicillin-streptomycin (Thermo Fischer Scientific; 10378-016). Cells were used for experiments before reaching passage 25. Cells were continuously profiled for contamination by assessment of extranuclear SiR-DNA staining.

Transfection

U2OS cells were seeded to reach 50–80% density on the day of transfection. DNA transfections were performed with Lipofectamine 2000 (11668; Thermo Fisher Scientific) in Opti-MEM (31985; Gibco) with DNA concentrations ranging from 50 to 300 ng DNA per cm^2 of growth surface. HeLa cells were transfected with 6 µg of plasmid using the Neon transfection device (Thermo Fisher) according to the manufacturer's instructions and parameter listed for HELA cells (2 pulses of 35 s at 1005 V). Cells were imaged after 24 h.

Live-cell imaging

For live imaging, cells were plated in µ-Slide 8 Well Glass Bottom chamber (80827; ibidi). Samples were imaged in a CO2-, temperature-, and humidity-controlled Tokai Hit Stage Top Incubator. The imaging media used was DMEM supplemented with 10% FBS and 1% antibiotic-antimycotic (15240112; Gibco). For SiR-DNA staining, cells were incubated with 250 nM SiR-DNA(Lukinavičius et al., 2015; Sen et al., 2018) in the growth media for 1 hr prior imaging.

Microscopy

Live cell imaging was also performed on an inverted Nikon Ti Eclipse microscope equipped with a Yokogawa CSU-W1 confocal scanner unit with solid state 100 mW 405, 488, 514, 594, 561, 594, and 640 nm lasers, using a 60× 1.4 NA plan Apo oil immersion objective lens and/or 20× plan Fluor 0.75 NA multi-

immersion objective lens, and a prime BSI sCMOS camera. GUV imaging was performed on an inverted Nikon Ti microscope equipped with a Yokogawa CSU-X1 confocal scanner unit with solid state 100mW 488-nm and 50-mW 561-nm lasers, using a 60× 1.4 NA plan Apo oil immersion objective lens, and a Hamamatsu ORCA R-2 Digital CCD Camera.

Hypotonic treatment

After taking images of cells in the isotonic condition (i.e., cultured in regular media), the medium was changed to a mixture of 150 µL of cell culture media and 150 µL of MilliQ water (resulting in approximately 150 mOSM). Cells were imaged immediately after the medium change within around 3 minutes.

Preparation of stretchable membranes

Stretchable polydimethylsiloxane (Sylgard Silicone Elastomer Kit, Dow Corning) membranes were prepared as previously described(Casares et al., 2015; Kosmalska et al., 2015). Briefly, a mix of 10:1 base to crosslinker ratio was degassed and spin-coated for 1 min at 500 rpm and cured at 65 °C overnight on methacrylate plates. Once polymerized, membranes were peeled off and assembled onto a metal ring that can subsequently be assembled in the stretch device.

Mechanical stimulation of the cells and live imaging

Cell mechanical stimulation was done as previously described using a custom-built stretching device that produced uniform biaxial deformations of stretchable PDMS membranes and of the overlying cells(Kosmalska et al., 2015). Briefly, a 150 µL droplet of a 10 µg/mL fibronectin solution (Sigma, F1141) was deposited at the center of the membrane mounted in the ring. After overnight incubation at 4 °C, the fibronectin solution was rinsed with PBS (Gibco, 14200-067), cells were seeded on the fibronectin-coated membranes and allowed to attach during 30–90 min in presence of Spy650-DNA (1:1000 dilution, Spirochrome, SC501). Before the experiment, the media was exchanged to CO2-independent media supplemented with rutin (Bogdanov et al., 2012). Then ring-containing membranes were mounted in the

stretch system previously described(Casares et al., 2015; Kosmalska et al., 2015). The stretch system was mounted inside of an inverted microscope (Nikon Eclipse Ti) equipped with an incubation chamber, and the temperature was kept et 37C during the experiment. Image of cells were acquired with a 60x objective (NIR Apo 60X/WD 2.8, Nikon) in the inverted microscope, with a spinning disk confocal unit (CSU-W1, Yokogawa), a Zyla sCMOS camera (Andor) and using the Micromanager software. For each cell, a stack of the nuclei at rest (0.2um step) was recorded using 488 nm (mNeon-green fluorescence) and 640 nm (SpyDNA fluorescence) excitation wavelengths. Several cells (5-6) were imaged in this condition at rest (before stretching) and their positions were recorded. The PDMS substrate was stretched (12-15% substrate strain), the same cells were focused back after substrate movement due to stretch, and their nuclei were imaged in the stretched state in the same conditions.

Image analysis

"NE enrichment score" was quantified with a custom ImageJ Macro with a modification from our previous work(Lee et al., 2023) (see Fig. S11A for the workflow). After channels were split to SiR-DNA and AH-mNG-NLS images, the SiR-DNA image was auto-segmented by Li method to a binary image, which was used to obtain the ROI and measure the total intensity of "whole nucleus" region in the AH-mNG-NLS image. Then, the binary image of SiR-DNA was eroded three times and used to mask the AH-mNG image to measure the intensity of "Intra-nucleus". The intensity in "Nuclear rim" was obtained by subtraction of the values of "Intra-nucleus" from "Whole nucleus." Mean value of "Whole nucleus" and "Nuclear rim" were calculated by dividing the total intensity by the area of each. Finally, after subtraction of background mean value, the ratio of "Nuclear rim" to "Intra-nucleus" was calculated to give the "NE enrichment score."

The AH-GFP protein binding on GUV was quantified with a custom ImageJ macro. See Fig. S11B for an illustration of the ROIs mentioned below. After the channels were split to GUV and AH-GFP images, the GUV image was auto-segmented by Li method and was used to obtain the ROI #1. Then, the segmented image was eroded two times and used to obtain ROI #2. The intensity of AH-GFP in ROI #2 was subtracted from that in ROI#1 to obtain the value of "GUV rim". ROI #2 was then eroded three more times to obtain

ROI #3, which was used to obtain a background value. ROI #3 was then dilated 10 and 15 times to define ROIs #4 and #5, respectively. Subtraction of the AH-GFP intensity in ROI #4 from that in ROI #5 was performed to obtain the AH-GFP intensity in "Outside of GUV". After subtraction of the background intensity value, the ratio between "GUV rim" to "Outside of GUV" was obtained.

D factor

D factor was given by: D = 0.944 * μH + 0.33 * z, where μH is the magnitude of hydrophobic moment and z is the net charge of a given AH, accordingly to HeliQuest (https://heliquest.ipmc.cnrs.fr/HelpProcedure.htm" \l "heading3).

Mapping AH amino acid compositions

The analysis was performed with custom Python scripts found on Github (https://github.com/shokenlee/AH_AAcomposition) inspired by HeliQuest. Firstly, each amino acid residue was placed in a wheel projection with an assumption that all of the AHs are α-helix and rotates 100 degree per residue (3.6 residues per turn). Then, the direction and magnitude of the mean hydrophobic moment was calculated using the standard hydrophobicity scale(Fauchere and Pliska, 1983). The hydrophobic and hydrophilic faces were determined by the direction of the mean hydrophobic moment vector such that the vector is oriented to the middle (90 degrees from each end) of the hydrophilic face. Then, the amino acid composition for each face was determined.

Immunoblot

Cells in a 24 well plate were lysed with 50 μL of ice-cold RIPA buffer (25 mM Tris pH 7.4,1% NP-40, 0.5% sodium deoxycholate, 0.1% SDS, 150 mM NaCl,and 1 tablet/50 ml cOmplete Mini protease inhibitor cocktail[11836153001; Roche]), incubated on ice for 15 min, and then centrifuged at >20,000 × g (15,000 rpm) for15 min at 4°C. Eighteen microliter of whole cell lysates/lane were run on 8–15% polyac-rylamide gels dependent on target size, and protein was wet-transferred to 0.22 μm nitrocellulose membranes

(1620112; Bio-Rad). Membranes were blocked in 1% BSA in PBS for 30 min. Membranes were then incubated with primary antibodies in BSA for 1.5 h at room temperature or over-night at 4°C with rocking. Membranes were washed three times for 5 min in TBST, then incubated with goat anti-mouse IgG secondary antibodies (31430; Thermo Fisher Scientific) in 5% milk in TBST for 45 min at room temperature with rocking. Membranes were washed three times for 5 min in TBST. Clarity ECL reagent (1705060S; Bio-Rad) or ECL select (RPN2235; Cytiva) was used to visualize chemiluminescence, and images were taken with a Bio-Rad ChemiDoc Imaging System. Antibody concentration was the following: anti-mNG 1:3,000; α-tubulin1:5,000; secondary antibodies 1:10,000.

Recombinant protein purification

6xHis-SUMO-AH-GFP proteins were expressed in Escherichia coli BL21(DE3) cells. Cells were grown at 37 °C to an OD 600nm of 0.4-0.7 and then cooled at 20 °C. Protein expression was induced with 0.1 mM isopropyl βD-1-thiogalactopyranoside (IPTG) at 20 °C for 16 h, and cells were harvested by centrifugation and stored at −80 °C. Frozen cells were resuspended in lysis buffer (50 mM Na_2HPO_4, 500 mM NaCl, 10 mM imidazole, pH 8.0) and lysed by sonication. After adding betamercaptoethanol at final 10 mM, sample was centrifuged at 21,000 g at 4 °C for 20 min. The supernatant was incubated with pre-equilibrated Ni-NTA agarose (Qiagen 30210) at 4 °C for 1 h. The resin was centrifuged at 2,000 rpm at 4 °C for 2 min, washed 3 times with wash buffer (50 mM Na_2HPO_4, 300 mM NaCl, 20 mM imidazole, pH 8.0). Protein was eluted with elution buffer (50 mM Na_2HPO_4, 300 mM NaCl, 250 mM imidazole, pH 8.0), aliquoted and analyzed by SDS-PAGE and Coomassie blue stain. Fractions containing the protein were collected and 6xHis-SUMO was cleaved by treatment with recombinant 6xHis-Ulp1 (a gift from Li-Tao Guo, Yale University) at 4°C for 1 h. 6xHis-SUMO and 6xHis-Ulp1 was removed by incubation with Ni-NTA agarose. AH-GFP protein was buffer-exchanged with 1xPBS by using Amicon centrifugal filter MWCO 10 kDa (Millipore Sigma Cat# UFC5010), then flash-frozen and stored at -80 °C until used.

Preparation and imaging of giant unilamellar vesicles

GUVs were prepared by polyvinyl alcohol (PVA)-assisted swelling (Romanauska and Köhler, 2023; Weinberger et al., 2013). PVA (weight-average molecular weight of 146,000 to 186,000; Cat# 363065; Sigma-Aldrich) was solubilized in water 5% (w/w) stirred and heated at 90 °C for 1 hr and stored at room temperature until used. Fourty microliters of PVA solution was spread on a glass coverslip (1.2 cm diameter), which was pre-washed with 70% ethanol and distilled water, and dried at 50 °C for 30 min. PVA coated coverslips were stored at room temperature until used. Two microliters of lipid mixture (1 mg/ml) in chloroform was spread on top of the PVA layer and chloroform was allowed to evaporate for 1 h. Two-hundred microliters of swelling solution (280 mM sucrose) was added on the coverslip in 24 well cell culture plate and incubated for 1 h at room temperature with gentle rocking to induce vesicle formation. Vesicles were collected by pipetting and centrifuged at 500 g for 5 min. Supernatant was discarded and vesicles in pellet was suspended in 1xPBS and kept at room temperature for immediate use. Vesicles were mixed with AH-GFP proteins (final concentration 500 nM) and immediately imaged in ibidi 8 well chamber in confocal microscope as described above. Wells were blocked for 1 h with 2.5 mg ml−1 bovine serum albumin in PBS and were washed with 1xPBS before loading the samples.

In silico prediction of ΔΔF values

ΔΔF values were predicted for each AH by using PMIpred(van Hilten et al., 2024) with neutral membrane as the target.

Statistical analysis

GraphPad Prism 8 was used for all statistical analysis otherwise specified in methods. Statistical tests used, sample sizes, definitions of n and N, and p values are reported in Figures and/or Figure legends.

References

Abe, Y., T. Shodai, T. Muto, K. Mihara, H. Torii, S. Nishikawa, T. Endo, and D. Kohda. 2000. Structural basis of presequence recognition by the mitochondrial protein import receptor Tom20. *Cell*. 100:551-560.

Amm, I., M. Weberruss, A. Hellwig, J. Schwarz, M. Tatarek-Nossol, C. Lüchtenborg, M. Kallas, B. Brügger, E. Hurt, and W. Antonin. 2023. Distinct domains in Ndc1 mediate its interaction with the Nup84 complex and the nuclear membrane. *J Cell Biol*. 222.

Andreu, I., I. Granero-Moya, N.R. Chahare, K. Clein, M. Molina-Jordán, A.E.M. Beedle, A. Elosegui-Artola, J.F. Abenza, L. Rossetti, X. Trepat, B. Raveh, and P. Roca-Cusachs. 2022. Mechanical force application to the nucleus regulates nucleocytoplasmic transport. *Nat Cell Biol*. 24:896-905.

Bahmanyar, S., and C. Schlieker. 2020. Lipid and protein dynamics that shape nuclear envelope identity. *Mol Biol Cell*. 31:1315-1323.

Baird, M.A., R.S. Fischer, C.E. Jewett, D. Malide, A.X. Cartagena-Rivera, and C.M. Waterman. 2023. Lamin B Receptor Upregulation in Metastatic Melanoma Causes Cholesterol-Mediated Nuclear Envelope Fragility. *bioRxiv*:2023.2012.2021.572889.

Barbosa, A.D., K. Lim, M. Mari, J.R. Edgar, L. Gal, P. Sterk, B.J. Jenkins, A. Koulman, D.B. Savage, M. Schuldiner, F. Reggiori, P.A. Wigge, and S. Siniossoglou. 2019. Compartmentalized Synthesis of Triacylglycerol at the Inner Nuclear Membrane Regulates Nuclear Organization. *Dev Cell*. 50:755-766.e756.

Bigay, J., and B. Antonny. 2012. Curvature, lipid packing, and electrostatics of membrane organelles: defining cellular territories in determining specificity. *Dev Cell*. 23:886-895.

Bigay, J., J.F. Casella, G. Drin, B. Mesmin, and B. Antonny. 2005. ArfGAP1 responds to membrane curvature through the folding of a lipid packing sensor motif. *EMBO J*. 24:2244-2253.

Bindels, D.S., L. Haarbosch, L. van Weeren, M. Postma, K.E. Wiese, M. Mastop, S. Aumonier, G. Gotthard, A. Royant, M.A. Hink, and T.W. Gadella. 2017. mScarlet: a bright monomeric red fluorescent protein for cellular imaging. *Nat Methods*. 14:53-56.

Bogdanov, A.M., E.I. Kudryavtseva, and K.A. Lukyanov. 2012. Anti-fading media for live cell GFP imaging. *PLoS One*. 7:e53004.

Brady, J.P., J.K. Claridge, P.G. Smith, and J.R. Schnell. 2015. A conserved amphipathic helix is required for membrane tubule formation by Yop1p. *Proc Natl Acad Sci U S A*. 112:E639-648.

Breeze, E., N. Dzimitrowicz, V. Kriechbaumer, R. Brooks, S.W. Botchway, J.P. Brady, C. Hawes, A.M. Dixon, J.R. Schnell, M.D. Fricker, and L. Frigerio. 2016. A C-terminal amphipathic helix is necessary for the in vivo tubule-shaping function of a plant reticulon. *Proc Natl Acad Sci U S A*. 113:10902-10907.

Carley, E., R.M. Stewart, A. Zieman, I. Jalilian, D.E. King, A. Zubek, S. Lin, V. Horsley, and M.C. King. 2021. The LINC complex transmits integrin-dependent tension to the nuclear lamina and represses epidermal differentiation. *Elife*. 10.

Casares, L., R. Vincent, D. Zalvidea, N. Campillo, D. Navajas, M. Arroyo, and X. Trepat. 2015. Hydraulic fracture during epithelial stretching. *Nat Mater*. 14:343-351.

Cheng, L.C., S. Baboo, C. Lindsay, L. Brusman, S. Martinez-Bartolomé, O. Tapia, X. Zhang, J.R. Yates, and L. Gerace. 2019. Identification of new transmembrane proteins concentrated at the nuclear envelope using organellar proteomics of mesenchymal cells. *Nucleus*. 10:126-143.

Cheng, L.C., X. Zhang, S. Baboo, J.A. Nguyen, S. Martinez-Bartolomé, E. Loose, J. Diedrich, J.R. Yates, and L. Gerace. 2023. Comparative membrane proteomics reveals diverse cell regulators concentrated at the nuclear envelope. *Life Sci Alliance*. 6.

Chua, N.K., V. Howe, N. Jatana, L. Thukral, and A.J. Brown. 2017. A conserved degron containing an amphipathic helix regulates the cholesterol-mediated turnover of human squalene monooxygenase, a rate-limiting enzyme in cholesterol synthesis. *J Biol Chem*. 292:19959-19973.

Čopič, A., S. Antoine-Bally, M. Giménez-Andrés, C. La Torre Garay, B. Antonny, M.M. Manni, S. Pagnotta, J. Guihot, and C.L. Jackson. 2018. A giant amphipathic helix from a perilipin that is adapted for coating lipid droplets. *Nat Commun*. 9:1332.

Cornell, R., and B. Antonny. 2018. CCTα Commands Phospholipid Homeostasis from the Nucleus. *Dev Cell*. 45:419-420.

Cornell, R.B. 2016. Membrane lipid compositional sensing by the inducible amphipathic helix of CCT. *Biochim Biophys Acta*. 1861:847-861.

Daigle, N., J. Beaudouin, L. Hartnell, G. Imreh, E. Hallberg, J. Lippincott-Schwartz, and J. Ellenberg. 2001. Nuclear pore complexes form immobile networks and have a very low turnover in live mammalian cells. *J Cell Biol*. 154:71-84.

Doucet, C.M., N. Esmery, M. de Saint-Jean, and B. Antonny. 2015. Membrane Curvature Sensing by Amphipathic Helices Is Modulated by the Surrounding Protein Backbone. *PLoS One*. 10:e0137965.

Drin, G., and B. Antonny. 2010. Amphipathic helices and membrane curvature. *FEBS Lett*. 584:1840-1847.

Drin, G., J.F. Casella, R. Gautier, T. Boehmer, T.U. Schwartz, and B. Antonny. 2007. A general amphipathic alpha-helical motif for sensing membrane curvature. *Nat Struct Mol Biol*. 14:138-146.

Elosegui-Artola, A., I. Andreu, A.E.M. Beedle, A. Lezamiz, M. Uroz, A.J. Kosmalska, R. Oria, J.Z. Kechagia, P. Rico-Lastres, A.L. Le Roux, C.M. Shanahan, X. Trepat, D. Navajas, S. Garcia-Manyes, and P. Roca-Cusachs. 2017. Force Triggers YAP Nuclear Entry by Regulating Transport across Nuclear Pores. *Cell*. 171:1397-1410.e1314.

Enyedi, B., M. Jelcic, and P. Niethammer. 2016. The Cell Nucleus Serves as a Mechanotransducer of Tissue Damage-Induced Inflammation. *Cell*. 165:1160-1170.

Ernst, R., C.S. Ejsing, and B. Antonny. 2016. Homeoviscous Adaptation and the Regulation of Membrane Lipids. *J Mol Biol*. 428:4776-4791.

Fauchere, J., and V. Pliska. 1983. Hydrophobic parameters {pi} of amino-acid sidechains from the partitioning of N-acetyl-amino-acid amides. *EUROPEAN JOURNAL OF MEDICINAL CHEMISTRY*. 18:369-375.

Feng, S.H., C.Q. Xia, P.D. Zhang, and H.B. Shen. 2022. Ab-Initio Membrane Protein Amphipathic Helix Structure Prediction Using Deep Neural Networks. *IEEE/ACM Trans Comput Biol Bioinform*. 19:795-805.

Foo, S., A. Cazenave-Gassiot, M.R. Wenk, and S. Oliferenko. 2023. Diacylglycerol at the inner nuclear membrane fuels nuclear envelope expansion in closed mitosis. *J Cell Sci*. 136.

Garcia, M., S. Kumanski, A. Elías-Villalobos, C. Cazevieille, C. Soulet, and M. Moriel-Carretero. 2022. Nuclear ingression of cytoplasmic bodies accompanies a boost in autophagy. *Life Sci Alliance*. 5.

Garten, M., C. Prévost, C. Cadart, R. Gautier, L. Bousset, R. Melki, P. Bassereau, and S. Vanni. 2015. Methyl-branched lipids promote the membrane adsorption of α-synuclein by enhancing shallow lipid-packing defects. *Phys Chem Chem Phys*. 17:15589-15597.

Gautier, R., D. Douguet, B. Antonny, and G. Drin. 2008. HELIQUEST: a web server to screen sequences with specific alpha-helical properties. *Bioinformatics*. 24:2101-2102.

Giménez-Andrés, M., A. Čopič, and B. Antonny. 2018. The Many Faces of Amphipathic Helices. *Biomolecules*. 8.

Gurskaya, N.G., A.F. Fradkov, N.I. Pounkova, D.B. Staroverov, M.E. Bulina, Y.G. Yanushevich, Y.A. Labas, S. Lukyanov, and K.A. Lukyanov. 2003. A colourless green fluorescent protein

homologue from the non-fluorescent hydromedusa Aequorea coerulescens and its fluorescent mutants. *Biochem J*. 373:403-408.

Haider, A., Y.C. Wei, K. Lim, A.D. Barbosa, C.H. Liu, U. Weber, M. Mlodzik, K. Oras, S. Collier, M.M. Hussain, L. Dong, S. Patel, A. Alvarez-Guaita, V. Saudek, B.J. Jenkins, A. Koulman, M.K. Dymond, R.C. Hardie, S. Siniossoglou, and D.B. Savage. 2018. PCYT1A Regulates Phosphatidylcholine Homeostasis from the Inner Nuclear Membrane in Response to Membrane Stored Curvature Elastic Stress. *Dev Cell*. 45:481-495.e488.

Halbleib, K., K. Pesek, R. Covino, H.F. Hofbauer, D. Wunnicke, I. Hänelt, G. Hummer, and R. Ernst. 2017. Activation of the Unfolded Protein Response by Lipid Bilayer Stress. *Mol Cell*. 67:673-684.e678.

Hamed, M., and W. Antonin. 2021. Dunking into the Lipid Bilayer: How Direct Membrane Binding of Nucleoporins Can Contribute to Nuclear Pore Complex Structure and Assembly. *Cells*. 10.

Hofbauer, H.F., M. Gecht, S.C. Fischer, A. Seybert, A.S. Frangakis, E.H.K. Stelzer, R. Covino, G. Hummer, and R. Ernst. 2018. The molecular recognition of phosphatidic acid by an amphipathic helix in Opi1. *J Cell Biol*. 217:3109-3126.

Holthuis, J.C., and A.K. Menon. 2014. Lipid landscapes and pipelines in membrane homeostasis. *Nature*. 510:48-57.

Jumper, J., R. Evans, A. Pritzel, T. Green, M. Figurnov, O. Ronneberger, K. Tunyasuvunakool, R. Bates, A. Žídek, A. Potapenko, A. Bridgland, C. Meyer, S.A.A. Kohl, A.J. Ballard, A. Cowie, B. Romera-Paredes, S. Nikolov, R. Jain, J. Adler, T. Back, S. Petersen, D. Reiman, E. Clancy, M. Zielinski, M. Steinegger, M. Pacholska, T. Berghammer, S. Bodenstein, D. Silver, O. Vinyals, A.W. Senior, K. Kavukcuoglu, P. Kohli, and D. Hassabis. 2021. Highly accurate protein structure prediction with AlphaFold. *Nature*. 596:583-589.

Kalukula, Y., A.D. Stephens, J. Lammerding, and S. Gabriele. 2022. Mechanics and functional consequences of nuclear deformations. *Nat Rev Mol Cell Biol*. 23:583-602.

Kayagaki, N., O.S. Kornfeld, B.L. Lee, I.B. Stowe, K. O'Rourke, Q. Li, W. Sandoval, D. Yan, J. Kang, M. Xu, J. Zhang, W.P. Lee, B.S. McKenzie, G. Ulas, J. Payandeh, M. Roose-Girma, Z. Modrusan, R. Reja, M. Sagolla, J.D. Webster, V. Cho, T.D. Andrews, L.X. Morris, L.A. Miosge, C.C. Goodnow, E.M. Bertram, and V.M. Dixit. 2021. NINJ1 mediates plasma membrane rupture during lytic cell death. *Nature*. 591:131-136.

Kefauver, J.M., A.B. Ward, and A. Patapoutian. 2020. Discoveries in structure and physiology of mechanically activated ion channels. *Nature*. 587:567-576.

Korfali, N., G.S. Wilkie, S.K. Swanson, V. Srsen, D.G. Batrakou, E.A. Fairley, P. Malik, N. Zuleger, A. Goncharevich, J. de Las Heras, D.A. Kelly, A.R. Kerr, L. Florens, and E.C. Schirmer. 2010. The leukocyte nuclear envelope proteome varies with cell activation and contains novel transmembrane proteins that affect genome architecture. *Mol Cell Proteomics*. 9:2571-2585.

Korfali, N., G.S. Wilkie, S.K. Swanson, V. Srsen, J. de Las Heras, D.G. Batrakou, P. Malik, N. Zuleger, A.R. Kerr, L. Florens, and E.C. Schirmer. 2012. The nuclear envelope proteome differs notably between tissues. *Nucleus*. 3:552-564.

Kosmalska, A.J., L. Casares, A. Elosegui-Artola, J.J. Thottacherry, R. Moreno-Vicente, V. González-Tarragó, M. Del Pozo, S. Mayor, M. Arroyo, D. Navajas, X. Trepat, N.C. Gauthier, and P. Roca-Cusachs. 2015. Physical principles of membrane remodelling during cell mechanoadaptation. *Nat Commun*. 6:7292.

Kralt, A., M. Wojtynek, J.S. Fischer, A. Agote-Aran, R. Mancini, E. Dultz, E. Noor, F. Uliana, M. Tatarek-Nossol, W. Antonin, E. Onischenko, O. Medalia, and K. Weis. 2022. An amphipathic helix in Brl1 is required for nuclear pore complex biogenesis in. *Elife*. 11.

Krogh, A., B. Larsson, G. von Heijne, and E.L. Sonnhammer. 2001. Predicting transmembrane protein topology with a hidden Markov model: application to complete genomes. *J Mol Biol*. 305:567-580.

Lee, S., J.W. Carrasquillo Rodrı Guez, H. Merta, and S. Bahmanyar. 2023. A membrane-sensing mechanism links lipid metabolism to protein degradation at the nuclear envelope. *J Cell Biol*. 222.

Lemmon, M.A. 2008. Membrane recognition by phospholipid-binding domains. *Nat Rev Mol Cell Biol*. 9:99-111.

Lomakin, A.J., C.J. Cattin, D. Cuvelier, Z. Alraies, M. Molina, G.P.F. Nader, N. Srivastava, P.J. Sáez, J.M. Garcia-Arcos, I.Y. Zhitnyak, A. Bhargava, M.K. Driscoll, E.S. Welf, R. Fiolka, R.J. Petrie, N.S. De Silva, J.M. González-Granado, N. Manel, A.M. Lennon-Duménil, D.J. Müller, and M. Piel. 2020. The nucleus acts as a ruler tailoring cell responses to spatial constraints. *Science*. 370.

Lombardi, M.L., D.E. Jaalouk, C.M. Shanahan, B. Burke, K.J. Roux, and J. Lammerding. 2011. The interaction between nesprins and sun proteins at the nuclear envelope is critical for force transmission between the nucleus and cytoskeleton. *J Biol Chem*. 286:26743-26753.

Lu, J.P., Y. Wang, D.A. Sliter, M.M. Pearce, and R.J. Wojcikiewicz. 2011. RNF170 protein, an endoplasmic reticulum membrane ubiquitin ligase, mediates inositol 1,4,5-trisphosphate receptor ubiquitination and degradation. *J Biol Chem*. 286:24426-24433.

Lukinavičius, G., C. Blaukopf, E. Pershagen, A. Schena, L. Reymond, E. Derivery, M. Gonzalez-Gaitan, E. D'Este, S.W. Hell, D. Wolfram Gerlich, and K. Johnsson. 2015. SiR-Hoechst is a far-red DNA stain for live-cell nanoscopy. *Nat Commun*. 6:8497.

Mauro, M.S., G. Celma, V. Zimyanin, M.M. Magaj, K.H. Gibson, S. Redemann, and S. Bahmanyar. 2022. Ndc1 drives nuclear pore complex assembly independent of membrane biogenesis to promote nuclear formation and growth. *Elife*. 11.

Meinke, P., A.R.W. Kerr, R. Czapiewski, J.I. de Las Heras, C.R. Dixon, E. Harris, H. Kölbel, F. Muntoni, U. Schara, V. Straub, B. Schoser, M. Wehnert, and E.C. Schirmer. 2020. A multistage sequencing strategy pinpoints novel candidate alleles for Emery-Dreifuss muscular dystrophy and supports gene misregulation as its pathomechanism. *EBioMedicine*. 51:102587.

Mesmin, B., G. Drin, S. Levi, M. Rawet, D. Cassel, J. Bigay, and B. Antonny. 2007. Two lipid-packing sensor motifs contribute to the sensitivity of ArfGAP1 to membrane curvature. *Biochemistry*. 46:1779-1790.

Miroshnikova, Y.A., and S.A. Wickström. 2022. Mechanical Forces in Nuclear Organization. *Cold Spring Harb Perspect Biol*. 14.

Morita, E., J. Arii, D. Christensen, J. Votteler, and W.I. Sundquist. 2012. Attenuated protein expression vectors for use in siRNA rescue experiments. *Biotechniques*. 0:1-5.

Nava, M.M., Y.A. Miroshnikova, L.C. Biggs, D.B. Whitefield, F. Metge, J. Boucas, H. Vihinen, E. Jokitalo, X. Li, J.M. García Arcos, B. Hoffmann, R. Merkel, C.M. Niessen, K.N. Dahl, and S.A. Wickström. 2020. Heterochromatin-Driven Nuclear Softening Protects the Genome against Mechanical Stress-Induced Damage. *Cell*. 181:800-817.e822.

Niu, Y., J.G. Pemberton, Y.J. Kim, and T. Balla. 2024. Phosphatidylserine enrichment in the nuclear membrane regulates key enzymes of phosphatidylcholine synthesis. *EMBO J*. 43:3414-3449.

Nordeen, S.A., D.L. Turman, and T.U. Schwartz. 2020. Yeast Nup84-Nup133 complex structure details flexibility and reveals conservation of the membrane anchoring ALPS motif. *Nat Commun*. 11:6060.

Penfield, L., R. Shankar, E. Szentgyörgyi, A. Laffitte, M.S. Mauro, A. Audhya, T. Müller-Reichert, and S. Bahmanyar. 2020. Regulated lipid synthesis and LEM2/CHMP7 jointly control nuclear envelope closure. *J Cell Biol*. 219.

Pinot, M., S. Vanni, E. Ambroggio, D. Guet, B. Goud, and J.-B. Manneville. 2018. Feedback between membrane tension, lipid shape and curvature in the formation of packing defects. *bioRxiv*:389627.

Pranke, I.M., V. Morello, J. Bigay, K. Gibson, J.M. Verbavatz, B. Antonny, and C.L. Jackson. 2011. α-Synuclein and ALPS motifs are membrane curvature sensors whose contrasting chemistry mediates selective vesicle binding. *J Cell Biol*. 194:89-103.

Prévost, C., M.E. Sharp, N. Kory, Q. Lin, G.A. Voth, R.V. Farese, and T.C. Walther. 2018. Mechanism and Determinants of Amphipathic Helix-Containing Protein Targeting to Lipid Droplets. *Dev Cell*. 44:73-86.e74.

Reicher, A., J. Reiniš, M. Ciobanu, P. Růžička, M. Malik, M. Siklos, V. Kartysh, T. Tomek, A. Koren, A.F. Rendeiro, and S. Kubicek. 2024. Pooled multicolour tagging for visualizing subcellular protein dynamics. *Nat Cell Biol*. 26:745-756.

Romanauska, A., and A. Köhler. 2018. The Inner Nuclear Membrane Is a Metabolically Active Territory that Generates Nuclear Lipid Droplets. *Cell*. 174:700-715.e718.

Romanauska, A., and A. Köhler. 2021. Reprogrammed lipid metabolism protects inner nuclear membrane against unsaturated fat. *Dev Cell*. 56:2562-2578.e2563.

Romanauska, A., and A. Köhler. 2023. Lipid saturation controls nuclear envelope function. *Nat Cell Biol*. 25:1290-1302.

Samardak, K., J. Bâcle, and M. Moriel-Carretero. 2024. Behind the stoNE wall: A fervent activity for nuclear lipids. *Biochimie*.

Schindelin, J., I. Arganda-Carreras, E. Frise, V. Kaynig, M. Longair, T. Pietzsch, S. Preibisch, C. Rueden, S. Saalfeld, B. Schmid, J.Y. Tinevez, D.J. White, V. Hartenstein, K. Eliceiri, P. Tomancak, and A. Cardona. 2012. Fiji: an open-source platform for biological-image analysis. *Nat Methods*. 9:676-682.

Schirmer, E.C., L. Florens, T. Guan, J.R. Yates, and L. Gerace. 2003. Nuclear membrane proteins with potential disease links found by subtractive proteomics. *Science*. 301:1380-1382.

Sen, O., A.T. Saurin, and J.M.G. Higgins. 2018. The live cell DNA stain SiR-Hoechst induces DNA damage responses and impairs cell cycle progression. *Sci Rep*. 8:7898.

Shen, Z., K.T. Belcheva, M. Jelcic, K.L. Hui, A. Katikaneni, and P. Niethammer. 2022. A synergy between mechanosensitive calcium- and membrane-binding mediates tension-sensing by C2-like domains. *Proc Natl Acad Sci U S A*. 119.

Sołtysik, K., Y. Ohsaki, T. Tatematsu, J. Cheng, A. Maeda, S.Y. Morita, and T. Fujimoto. 2021. Nuclear lipid droplets form in the inner nuclear membrane in a seipin-independent manner. *J Cell Biol*. 220.

Song, X., S. Liu, W. Wang, Z. Ma, X. Cao, and M. Jiang. 2020. E3 ubiquitin ligase RNF170 inhibits innate immune responses by targeting and degrading TLR3 in murine cells. *Cell Mol Immunol*. 17:865-874.

Taniguchi, R., C. Orniacki, J.P. Kreysing, V. Zila, C.E. Zimmerli, S. Böhm, B. Turoňová, H.-G. Kräusslich, V. Doye, and M. Beck. 2024. Nuclear pores safeguard the integrity of the nuclear envelope. *bioRxiv*:2024.2002.2005.578890.

Thaller, D.J., D. Tong, C.J. Marklew, N.R. Ader, P.J. Mannino, S. Borah, M.C. King, B. Ciani, and C.P. Lusk. 2021. Direct binding of ESCRT protein Chm7 to phosphatidic acid-rich membranes at nuclear envelope herniations. *J Cell Biol*. 220:e202004222.

Thul, P.J., L. Åkesson, M. Wiking, D. Mahdessian, A. Geladaki, H. Ait Blal, T. Alm, A. Asplund, L. Björk, L.M. Breckels, A. Bäckström, F. Danielsson, L. Fagerberg, J. Fall, L. Gatto, C. Gnann, S. Hober, M. Hjelmare, F. Johansson, S. Lee, C. Lindskog, J. Mulder, C.M. Mulvey, P. Nilsson, P. Oksvold, J. Rockberg, R. Schutten, J.M. Schwenk, Å. Sivertsson, E. Sjöstedt, M. Skogs, C. Stadler, D.P. Sullivan, H. Tegel, C. Winsnes, C. Zhang, M. Zwahlen, A. Mardinoglu, F. Pontén, K. von Feilitzen, K.S. Lilley, M. Uhlén, and E. Lundberg. 2017. A subcellular map of the human proteome. *Science*. 356.

Tsuji, T., J. Cheng, T. Tatematsu, A. Ebata, H. Kamikawa, A. Fujita, S. Gyobu, K. Segawa, H. Arai, T. Taguchi, S. Nagata, and T. Fujimoto. 2019. Predominant localization of phosphatidylserine at the cytoplasmic leaflet of the ER, and its TMEM16K-dependent redistribution. *Proc Natl Acad Sci U S A*. 116:13368-13373.

Vamparys, L., R. Gautier, S. Vanni, W.F. Bennett, D.P. Tieleman, B. Antonny, C. Etchebest, and P.F. Fuchs. 2013. Conical lipids in flat bilayers induce packing defects similar to that induced by positive curvature. *Biophys J*. 104:585-593.

van Hilten, N., J. Methorst, N. Verwei, and H.J. Risselada. 2023. Physics-based generative model of curvature sensing peptides; distinguishing sensors from binders. *Sci Adv*. 9:eade8839.

van Hilten, N., K.S. Stroh, and H.J. Risselada. 2020. Membrane Thinning Induces Sorting of Lipids and the Amphipathic Lipid Packing Sensor (ALPS) Protein Motif. *Front Physiol*. 11:250.

van Hilten, N., K.S. Stroh, and H.J. Risselada. 2022. Efficient Quantification of Lipid Packing Defect Sensing by Amphipathic Peptides: Comparing Martini 2 and 3 with CHARMM36. *J Chem Theory Comput*. 18:4503-4514.

van Hilten, N., N. Verwei, J. Methorst, C. Nase, A. Bernatavicius, and H.J. Risselada. 2024. PMIpred: a physics-informed web server for quantitative protein-membrane interaction prediction. *Bioinformatics*. 40.

Vanni, S., H. Hirose, H. Barelli, B. Antonny, and R. Gautier. 2014. A sub-nanometre view of how membrane curvature and composition modulate lipid packing and protein recruitment. *Nat Commun*. 5:4916.

Vanni, S., L. Vamparys, R. Gautier, G. Drin, C. Etchebest, P.F. Fuchs, and B. Antonny. 2013. Amphipathic lipid packing sensor motifs: probing bilayer defects with hydrophobic residues. *Biophys J*. 104:575-584.

Venturini, V., F. Pezzano, F. Català Castro, H.M. Häkkinen, S. Jiménez-Delgado, M. Colomer-Rosell, M. Marro, Q. Tolosa-Ramon, S. Paz-López, M.A. Valverde, J. Weghuber, P. Loza-Alvarez, M. Krieg, S. Wieser, and V. Ruprecht. 2020. The nucleus measures shape changes for cellular proprioception to control dynamic cell behavior. *Science*. 370.

Vollmer, B., M. Lorenz, D. Moreno-Andrés, M. Bodenhöfer, P. De Magistris, S.A. Astrinidis, A. Schooley, M. Flötenmeyer, S. Leptihn, and W. Antonin. 2015. Nup153 Recruits the Nup107-160 Complex to the Inner Nuclear Membrane for Interphasic Nuclear Pore Complex Assembly. *Dev Cell*. 33:717-728.

Weinberger, A., F.C. Tsai, G.H. Koenderink, T.F. Schmidt, R. Itri, W. Meier, T. Schmatko, A. Schröder, and C. Marques. 2013. Gel-assisted formation of giant unilamellar vesicles. *Biophys J*. 105:154-164.

Wilkie, G.S., N. Korfali, S.K. Swanson, P. Malik, V. Srsen, D.G. Batrakou, J. de las Heras, N. Zuleger, A.R. Kerr, L. Florens, and E.C. Schirmer. 2011. Several novel nuclear envelope transmembrane proteins identified in skeletal muscle have cytoskeletal associations. *Mol Cell Proteomics*. 10:M110.003129.

Wright, F.A., J.P. Lu, D.A. Sliter, N. Dupré, G.A. Rouleau, and R.J. Wojcikiewicz. 2015. A Point Mutation in the Ubiquitin Ligase RNF170 That Causes Autosomal Dominant Sensory Ataxia Destabilizes the Protein and Impairs Inositol 1,4,5-Trisphosphate Receptor-mediated Ca2+ Signaling. *J Biol Chem*. 290:13948-13957.

Lee et al. Figure 1

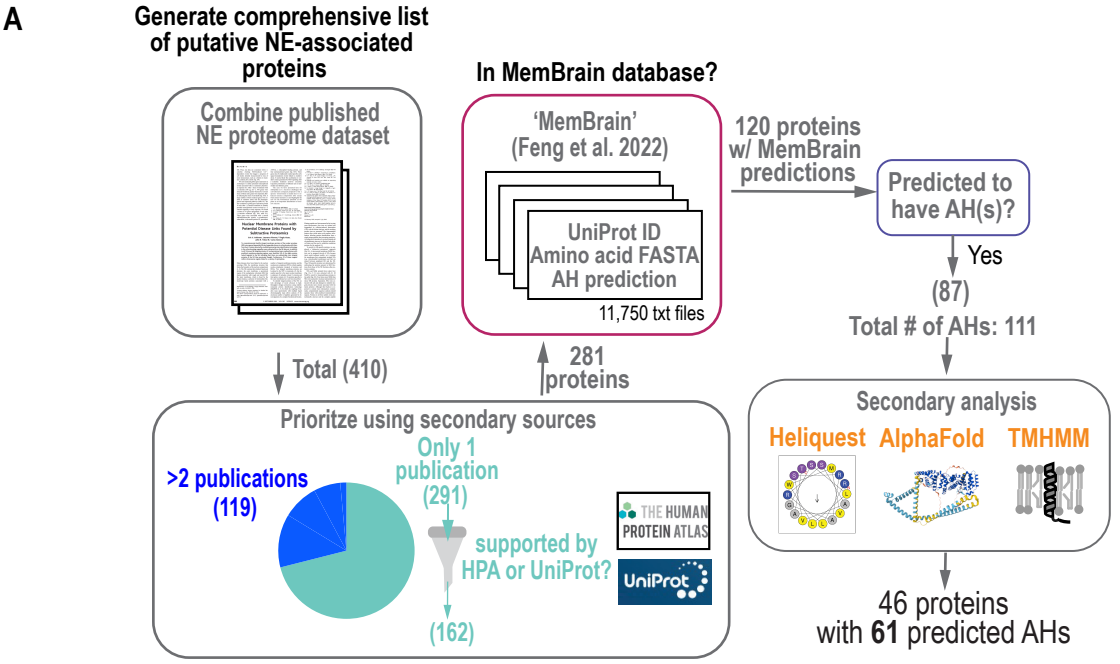

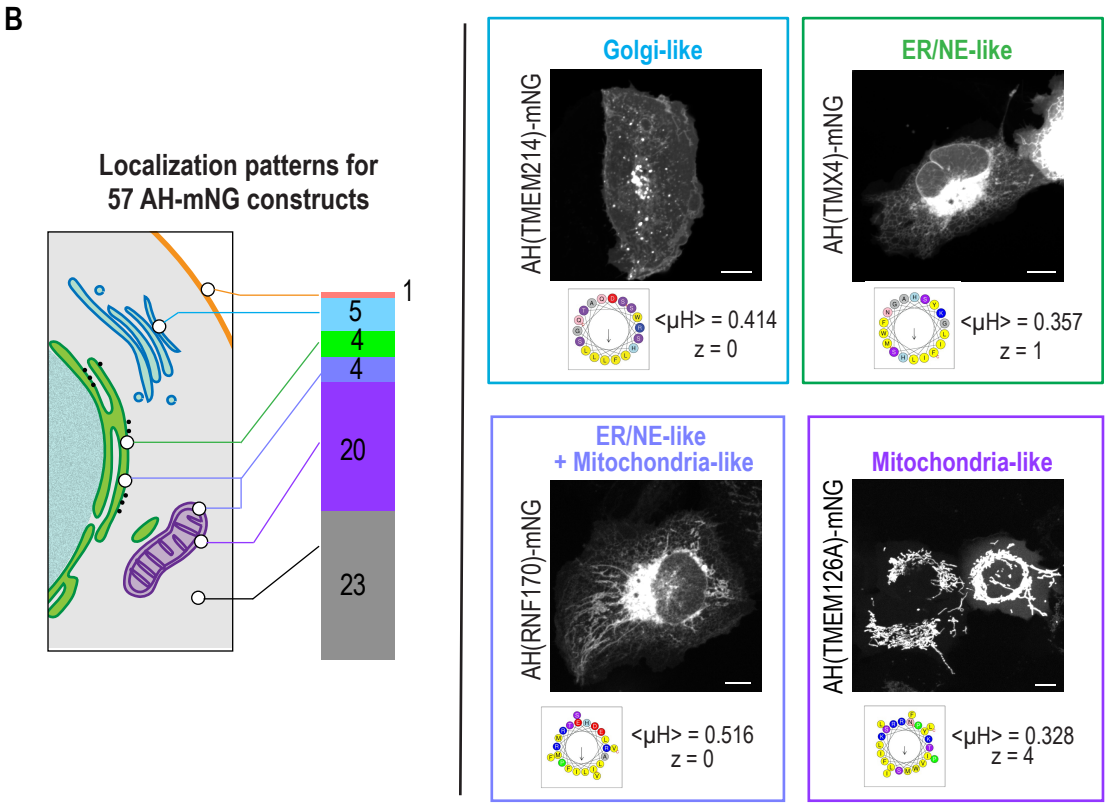

Fig. 1. Computational and cell biological screening for amphipathic helices in nuclear envelope resident proteins

(A) Workflow of the computational screening. See Fig. S1 for more detail. (B) AH-mNG screening by live cell imaging. Left, the organelle schematic denotes the plasma membrane (orange), Golgi (light blue), ER/NE (green), ER/NE + Mitochondria (light purple), Mitochondria (purple) and no detection of membranous-organelle localization (gray). Right, confocal images of live U2OS cells expressing the indicated constructs with a wheel projection of the AH and its mean hydrophobic moment <μH> and net charge z. See Fig. S2, S4 and S5 for representative images of other AH candidates. Scale bars, 10 μm.

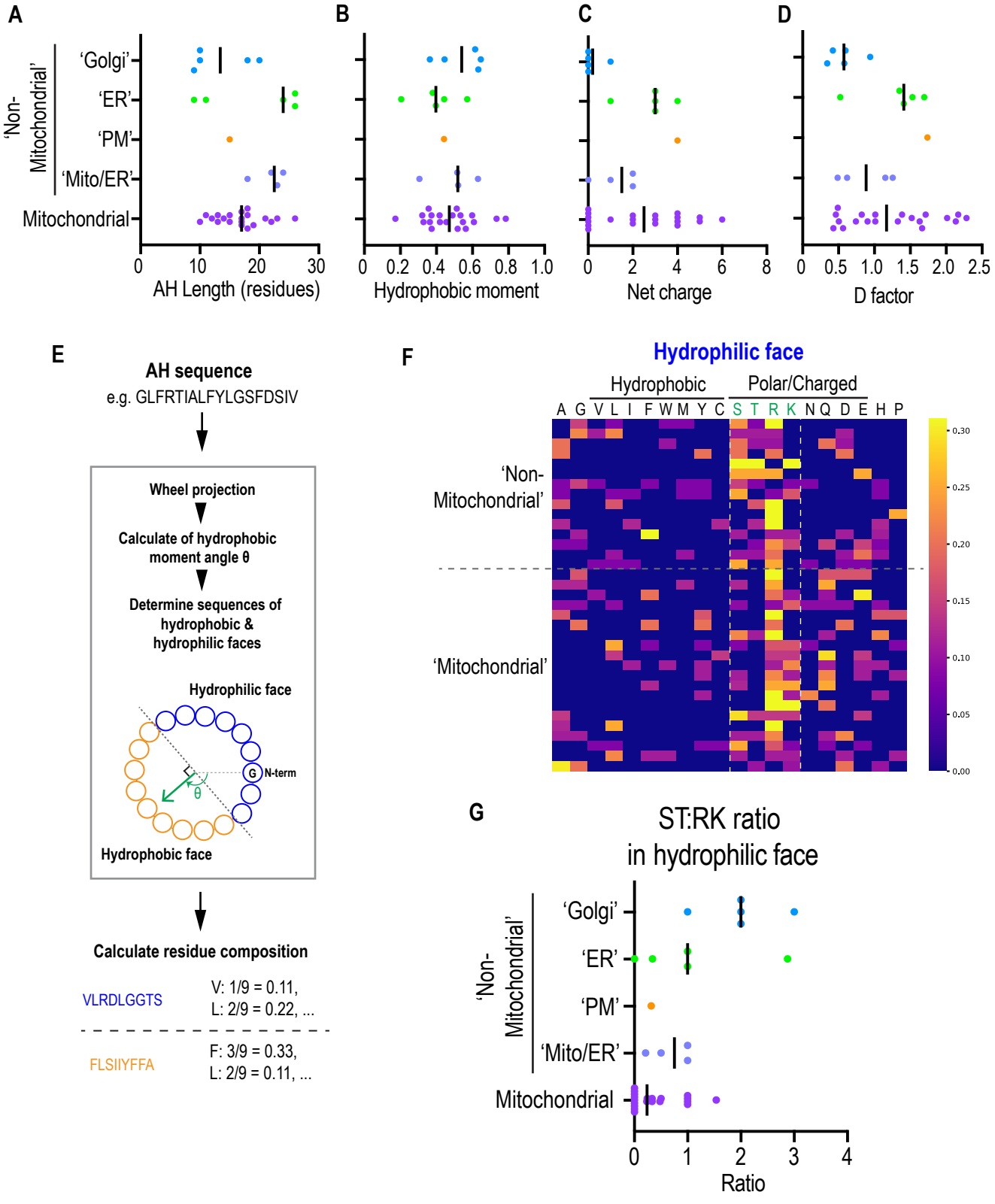
A
B
C
D
'Non-Mitochondrial'
'Golgi'
'ER'
'PM'
'Mito/ER'
Mitochondrial
0 10 20 30
AH Length (residues)
0 0.2 0.4 0.6 0.8 1.0
Hydrophobic moment
0 2 4 6 8
Net charge
0 0.5 1.0 1.5 2.0 2.5
D factor
E
AH sequence
e.g. GLFRTIALFYLGSFDSIV
Wheel projection
Calculate of hydrophobic moment angle θ
Determine sequences of hydrophobic & hydrophilic faces
Hydrophilic face
G
N-term
θ
Hydrophobic face
Calculate residue composition
VLRDLGGTS
V: 1/9 = 0.11,
L: 2/9 = 0.22, ...
FLSIIYFFA
F: 3/9 = 0.33,
L: 2/9 = 0.11, ...
F
Hydrophilic face
Hydrophobic
Polar/Charged
A G V L I F W M Y C S T R K N Q D E H P
'Non-Mitochondrial'
'Mitochondrial'
0.30
0.25
0.20
0.15
0.10
0.05
0.00
G
ST:RK ratio
in hydrophilic face
'Non-Mitochondrial'
'Golgi'
'ER'
'PM'
'Mito/ER'
Mitochondrial
0 1 2 3 4
Ratio

Fig. 2. Identification of a sequence code for the AH membrane preference

(A-D) Scatter plot of the indicated metrices of the AH candidates screened in Fig. 1B. Dots are color coded accordingly to the subcellular localization pattern in Fig. 1B. (E) Workflow of the amino acid composition analysis of the hydrophilic and hydrophobic faces of an AH. (F) Heatmap of the amino acid compositions in the hydrophilic face of AHs. Each raw represents an AH. (G) Scatter plot of the ratio of S/T residues to R/K residues in the hydrophilic face.

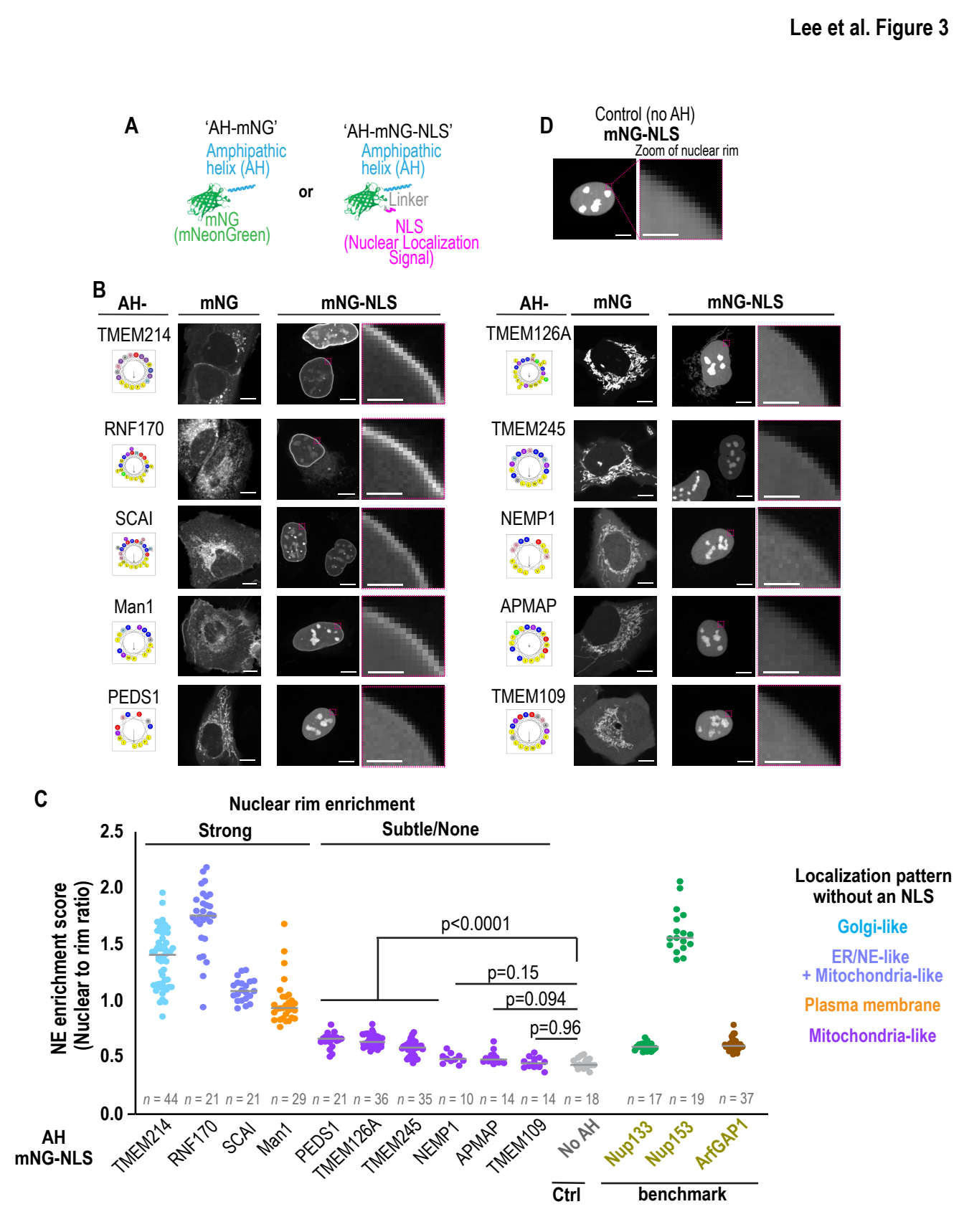
A
'AH-mNG'
Amphipathic helix (AH)
mNG (mNeonGreen)
or
'AH-mNG-NLS'
Amphipathic helix (AH)
Linker
NLS (Nuclear Localization Signal)
D
Control (no AH)
mNG-NLS
Zoom of nuclear rim
B
AH-
mNG
mNG-NLS
TMEM214
RNF170
SCAI
Man1
PEDS1
TMEM126A
TMEM245
NEMP1
APMAP
TMEM109
C
Nuclear rim enrichment
Strong
Subtle/None
NE enrichment score (Nuclear to rim ratio)
2.5
2.0
1.5
1.0
0.5
0.0
p<0.0001
p=0.15
p=0.094
p=0.96
n = 44 n = 21 n = 21 n = 29 n = 21 n = 36 n = 35 n = 10 n = 14 n = 14 n = 18 n = 17 n = 19 n = 37
AH mNG-NLS
TMEM214
RNF170
SCAI
Man1
PEDS1
TMEM126A
TMEM245
NEMP1
APMAP
TMEM109
No AH
Nup133
Nup153
ArfGAP1
Ctrl
benchmark
Localization pattern without an NLS
Golgi-like
ER/NE-like + Mitochondria-like
Plasma membrane
Mitochondria-like

Fig. 3. Subcellular localization pattern of AH-mNG correlates with the INM association propensity of the AH

(A) Schematic of the AH-mNG and AH-mNG-NLS constructs. (B) Confocal images of live U2OS cells expressing the indicated AH-mNG or AH-mNG-NLS constructs. Nuclear rim area was zoomed in. (C) NE enrichment score of the AH-mNG-NLS constructs. See Fig. S8 for representative images of AHs from Nup153, Nup133 and ArfGAP1. See Methods and Fig. S11 for details of the score quantification. Data points are from 2 or 3 experiments. Bars indicate median. p values: Welch and Brown-Forsythe ANOVA test. (D) Confocal images of live U2OS cells expressing mNG-NLS. Scale bars, 10 μm or 2 μm (zoom).

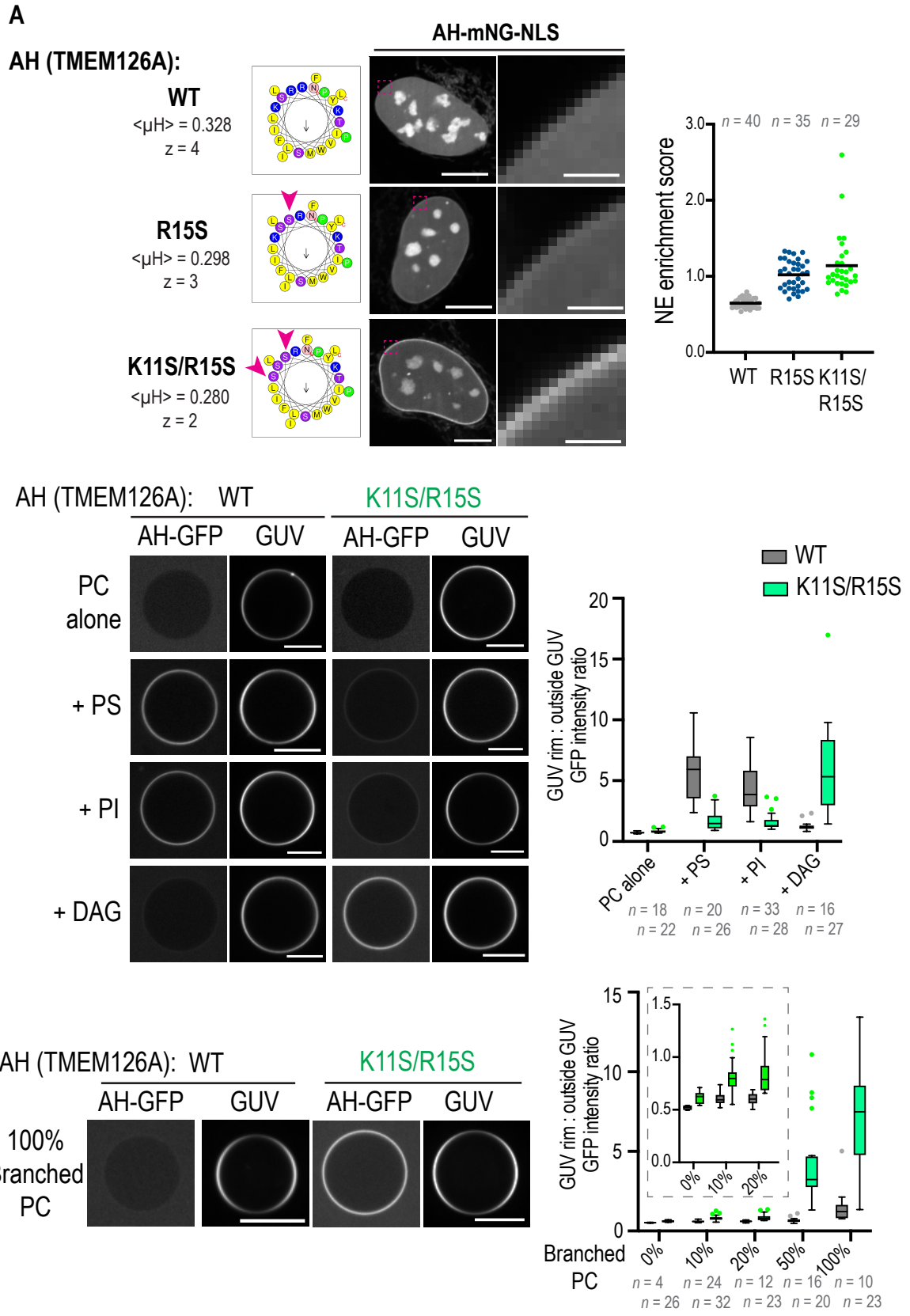
A
AH (TMEM126A):
AH-mNG-NLS
WT
<μH> = 0.328
z = 4
R15S
<μH> = 0.298
z = 3
K11S/R15S
<μH> = 0.280
z = 2
NE enrichment score
n = 40 n = 35 n = 29
WT
R15S
K11S/R15S
B
AH (TMEM126A): WT
K11S/R15S
AH-GFP
GUV
PC alone
+ PS
+ PI
+ DAG
GUV rim : outside GUV GFP intensity ratio
PC alone
+ PS
+ PI
+ DAG
n = 18 n = 20 n = 33 n = 16
n = 22 n = 26 n = 28 n = 27
C
AH (TMEM126A): WT
K11S/R15S
100% Branched PC
Branched PC
0%
10%
20%
50%
100%
n = 4 n = 24 n = 12 n = 16 n = 10
n = 26 n = 32 n = 23 n = 20 n = 23

Fig. 4. Reencoding of AH sequences informs on the physicochemical property of the INM

(A) Confocal images of live U2OS cells expressing the AH-mNG-NLS constructs and scatter plot of the NE enrichment scores. Data are pooled from two experiments. Scale bars, 10 µm or 2 µm (zoom). (B and C) Confocal images of GUVs with the indicated AH-GFP recombinant protein. Box plot shows the ratio of the AH-GFP intensity on GUV rim to outside GUV. In (C), Branched PC 0-20% plots are zoomed. Data are from 2 or 3 experiments. Scale bars, 10 µm.

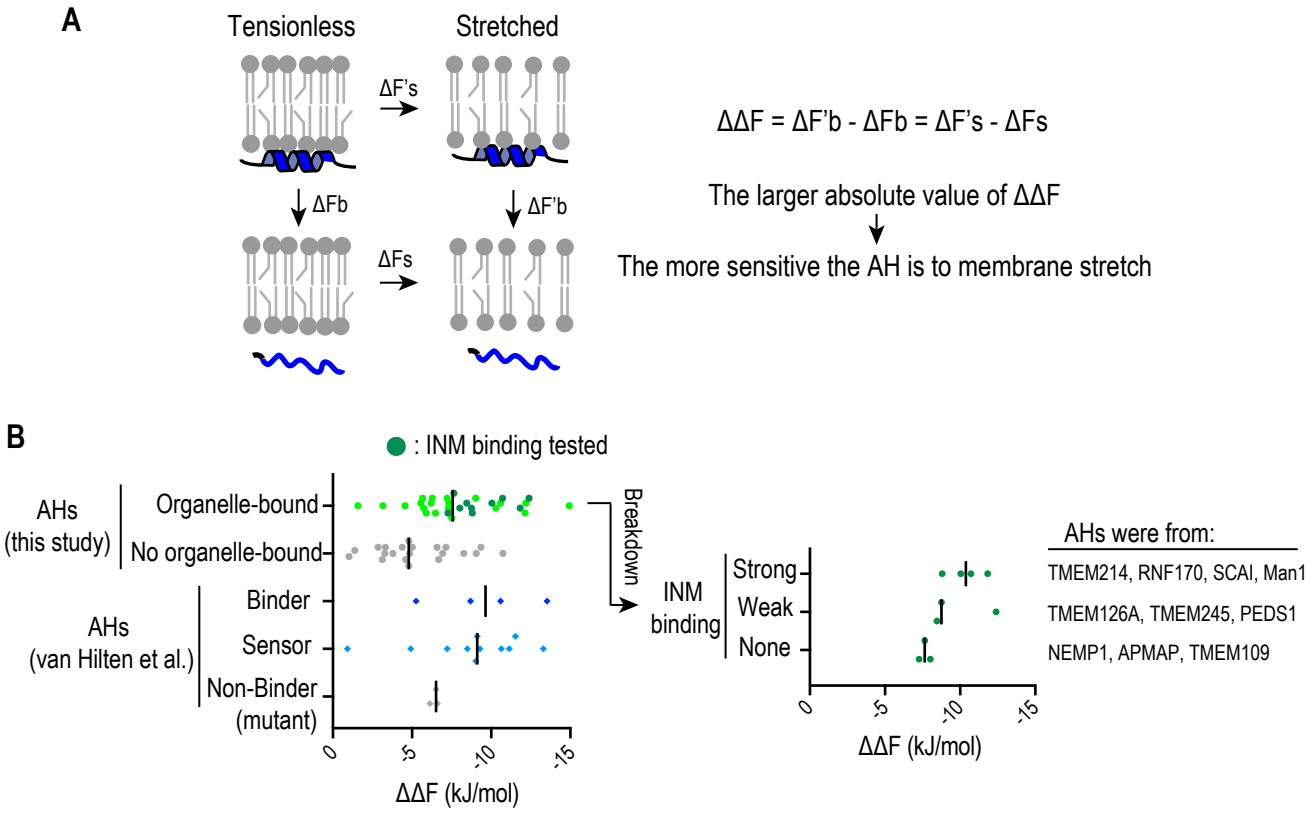
A
Tensionless
Stretched
ΔF's
ΔFb
ΔF'b
ΔFs
ΔΔF = ΔF'b - ΔFb = ΔF's - ΔFs
The larger absolute value of ΔΔF
The more sensitive the AH is to membrane stretch
B
: INM binding tested
AHs (this study)
Organelle-bound
No organelle-bound
AHs (van Hilten et al.)
Binder
Sensor
Non-Binder (mutant)
0
-5
-10
-15
ΔΔF (kJ/mol)
Breakdown
INM binding
Strong
Weak
None
ΔΔF (kJ/mol)
AHs were from:
TMEM214, RNF170, SCAI, Man1
TMEM126A, TMEM245, PEDS1
NEMP1, APMAP, TMEM109

Fig. 5. NE protein AHs are predicted to be sensitive to membrane tension

(A) Schematic of ΔΔF. Adopted from (van Hilten et al., 2022). (B) Left, ΔΔF values of AHs screened in Fig. 1B and AHs in (van Hilten et al. 2023) predicted by PMIpred. Right, ΔΔF values of AHs that were tested in AH-mNG-NLS constructs in Fig. 3. Bar in the plot indicates median.

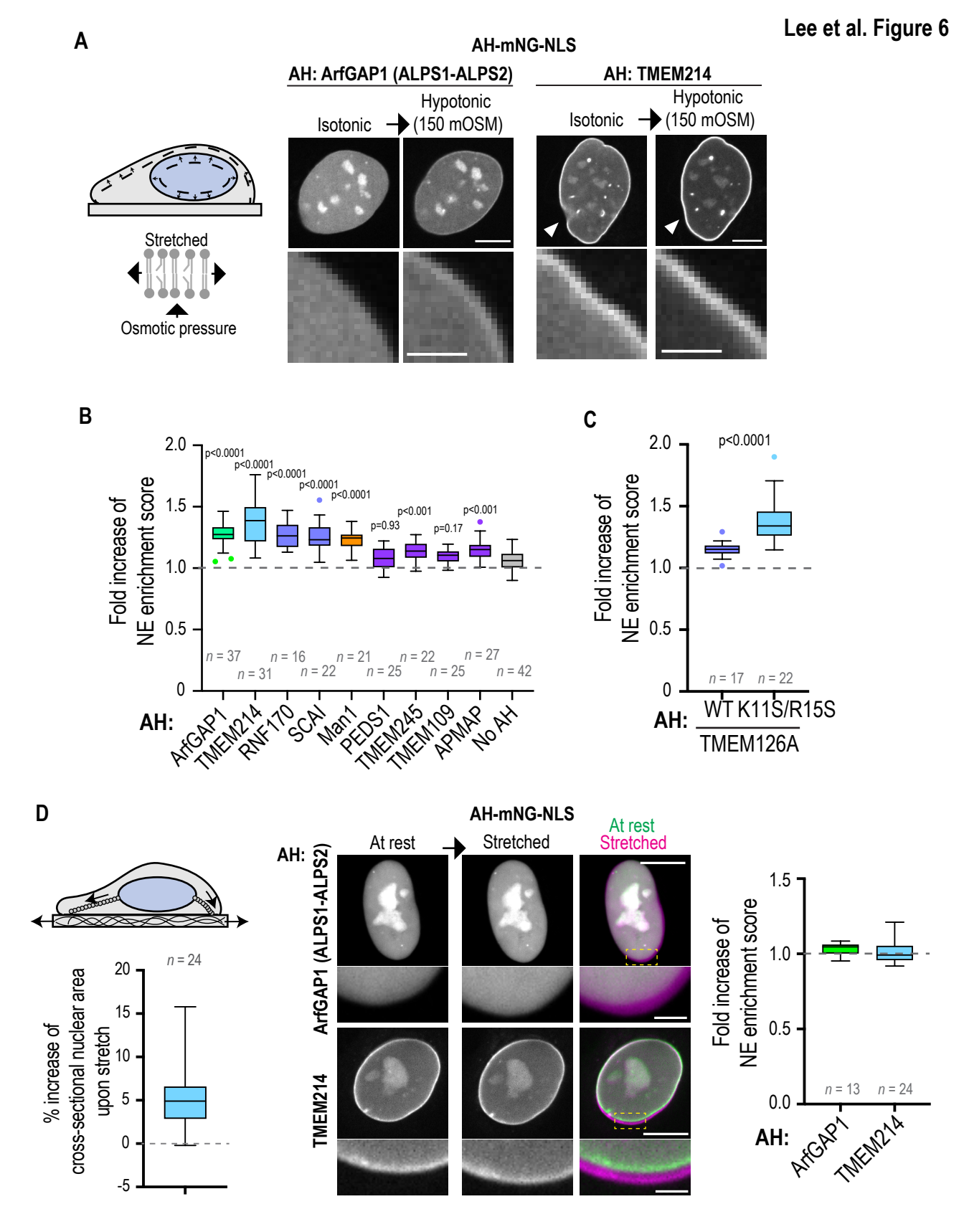
A
AH-mNG-NLS
AH: ArfGAP1 (ALPS1-ALPS2)
AH: TMEM214
Isotonic
Hypotonic (150 mOSM)
Stretched
Osmotic pressure
B
Fold increase of NE enrichment score
p<0.0001
p<0.0001
p<0.0001
p<0.0001
p<0.0001
p=0.93
p<0.001
p=0.17
p<0.001
n = 37
n = 31
n = 16
n = 22
n = 21
n = 25
n = 22
n = 25
n = 27
n = 42
AH:
ArfGAP1
TMEM214
RNF170
SCAI
Man1
PEDS1
TMEM245
TMEM109
APMAP
No AH
C
Fold increase of NE enrichment score
p<0.0001
n = 17
n = 22
AH:
WT
K11S/R15S
TMEM126A
D
AH-mNG-NLS
AH:
At rest
Stretched
At rest
Stretched
ArfGAP1 (ALPS1-ALPS2)
TMEM214
% increase of cross-sectional nuclear area upon stretch
n = 24
Fold increase of NE enrichment score
n = 13
n = 24
AH:
ArfGAP1
TMEM214

Fig. 6. NE protein AHs sense membrane stretch at the nuclear envelope

(A) Confocal images of live U2OS cells expressing the AH-mNG-NLS constructs before and after the hypotonic shock. An arrowhead indicates the deformation of the nucleus. (B and C) Fold increase of NE enrichment score of the indicated AH-mNG-NLS constructs upon hypotonic shock. Data are pooled from 2 experiments. P values against mNG-NLS ('No AH' control): Welch and Brown-Forsythe ANOVA test. (D) Left, Box plot of % increase of the cross-sectional nuclear area upon stretch. Right, Confocal images of live HeLa cells expressing the AH-mNG-NLS constructs before (at rest) and during stretch (stretched). Overlay of pseudo-colored images of nuclei before (green) or during (magenta) is shown. Box plot shows fold increase of NE enrichment score upon stretch. Data are pooled from 2 or 3 experiments. Scale bars, 10 µm or 2 µm (zoom).

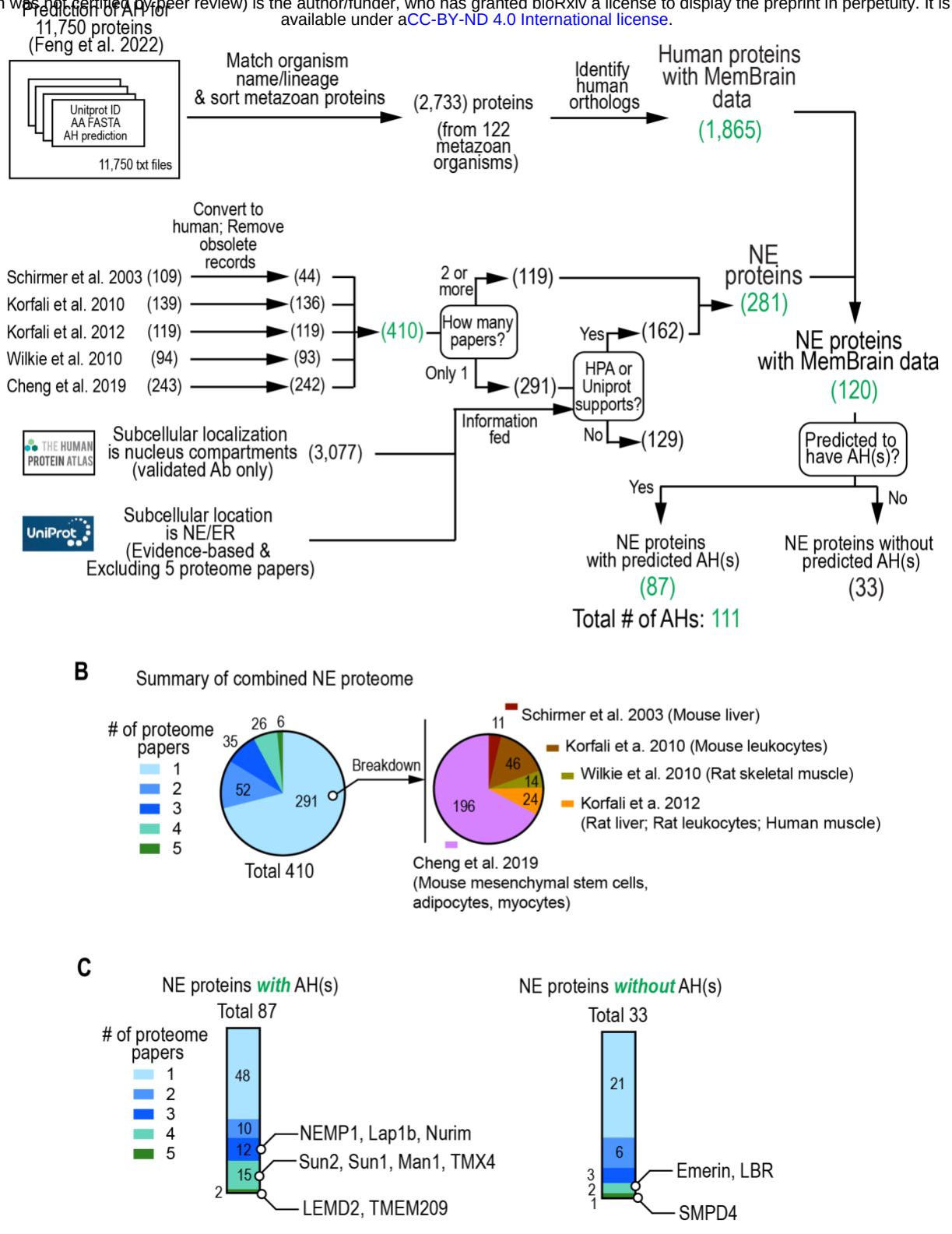

Fig. S1. Computational screen of AHs in nuclear envelope proteins.

(A) Workflow of the computational screen. Numbers in parenthesis indicate the number of proteins. (B) Pie chart of the 410 NE proteins by the number of the NE proteome papers. NE proteins that had only a single NE proteome papers were broken out by the NE proteome paper. (C) NE proteins with or without a predicted AH were broken out by the number of NE proteome papers.

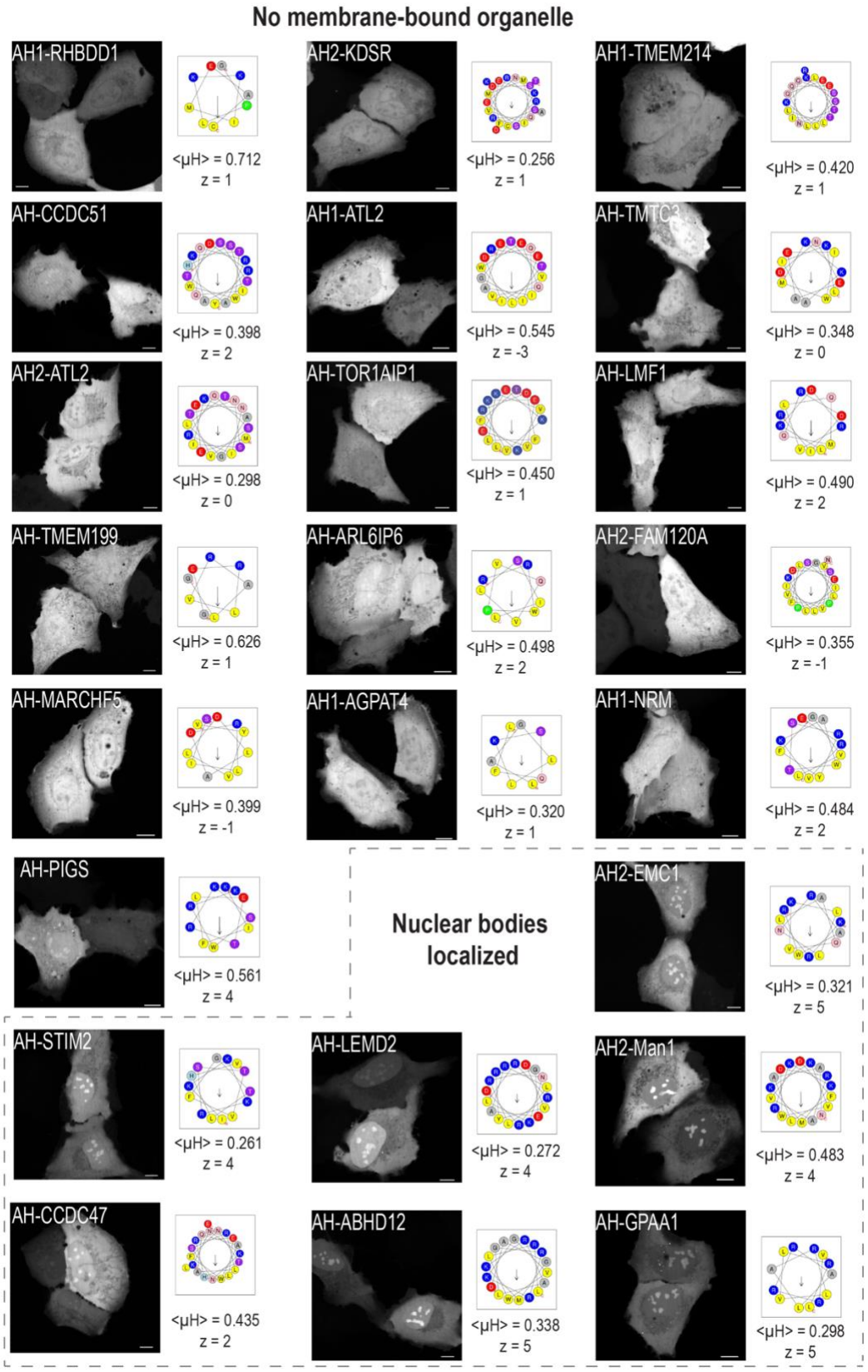

Fig. S2. Subcellular localization patterns of AH candidates tagged with mNG that did not localize to membrane-bound organelles.

Confocal images of live U2OS cells expressing the indicated AH-mNG constructs. AH-mNG with nuclear body-like pattern is highlighted at the bottom right. Scale bars, 10 μm.

Lee et al. Supplementary Figure 3

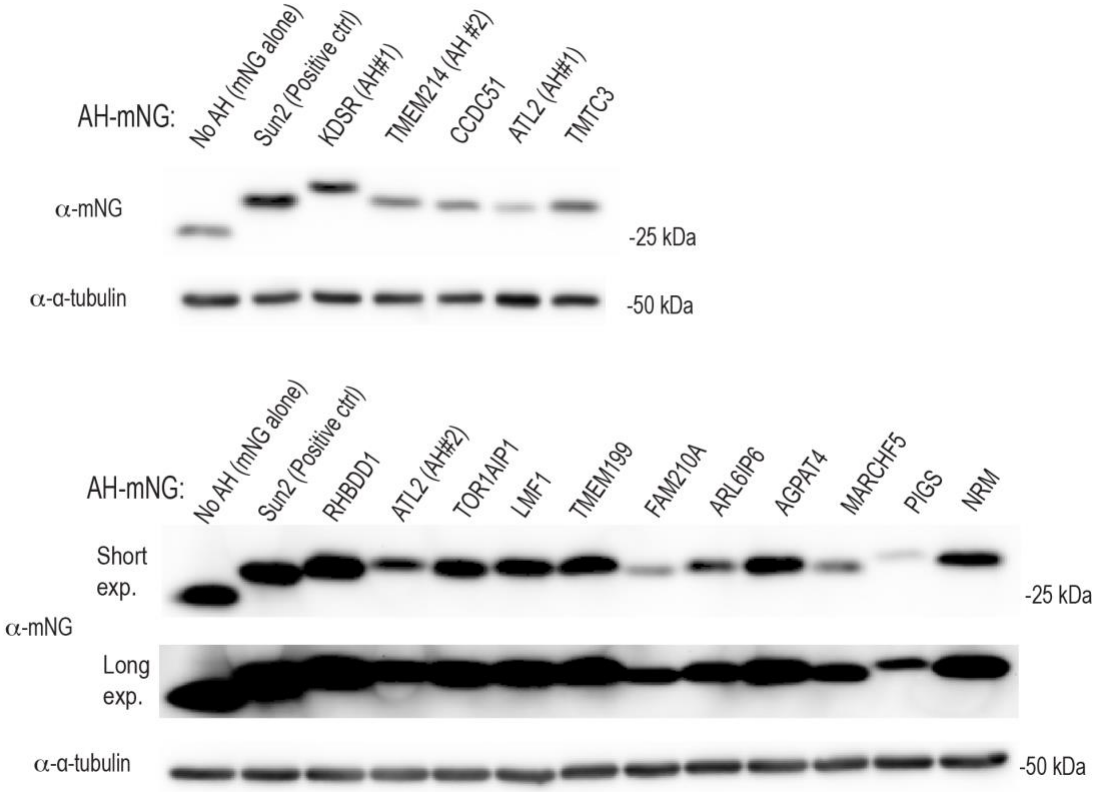

Fig. S3. AH-mNG without localization to membrane-bound organelle or nuclear bodies is expressed without unexpected cleavage of the AH.

Immunoblot of mNG alone or the indicated AH-mNG constructs transiently expressed in U2OS cells. Note that we tested only the AH-mNG constructs that did not localize to either membrane-bound organelles or nuclear bodies.

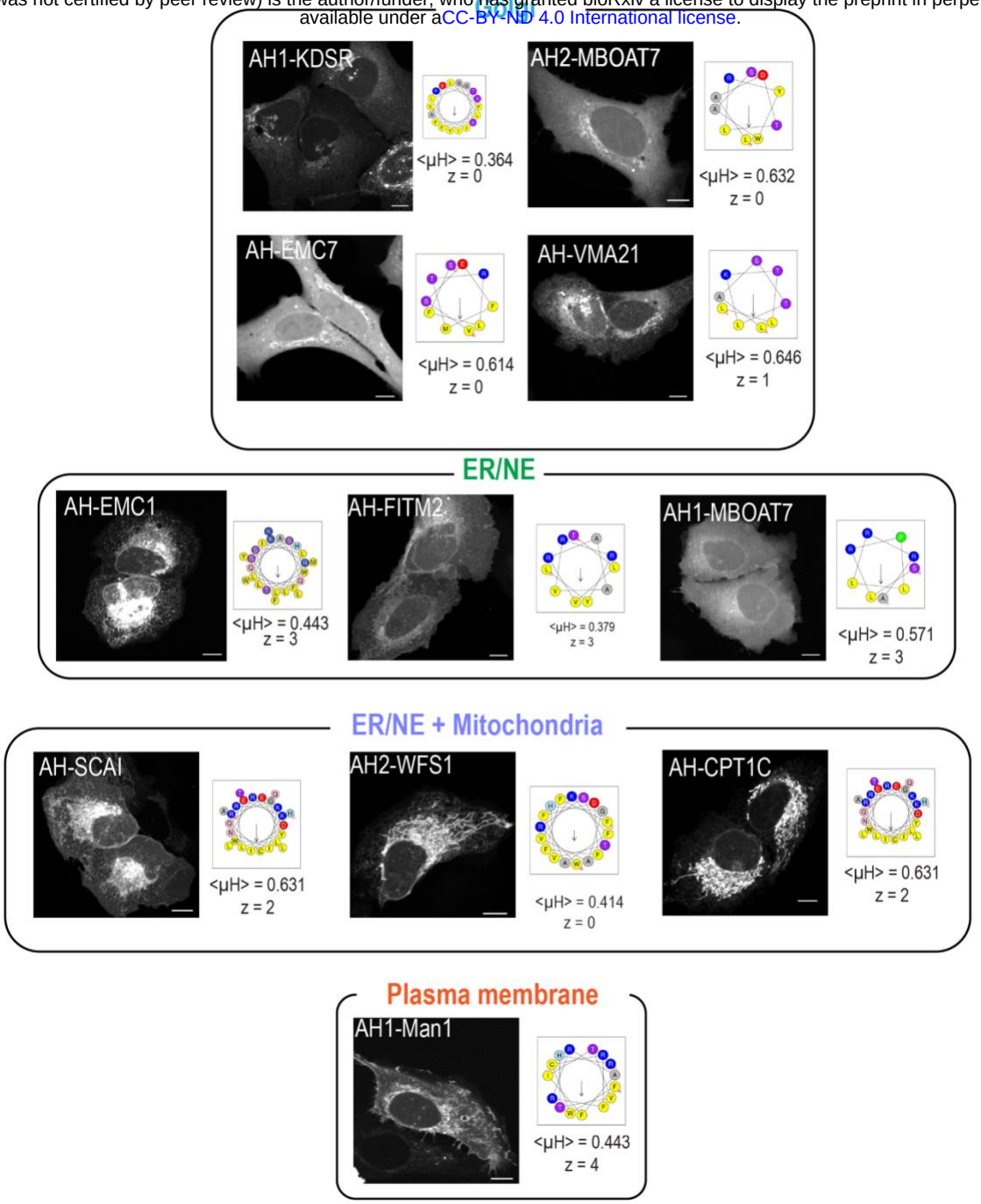

Fig. S4. Subcellular localization patterns of AH candidates tagged with mNG that displayed non-mitochondrial pattern.

Confocal images of live U2OS cells expressing the indicated AH-mNG constructs. Scale bars, 10 μm.

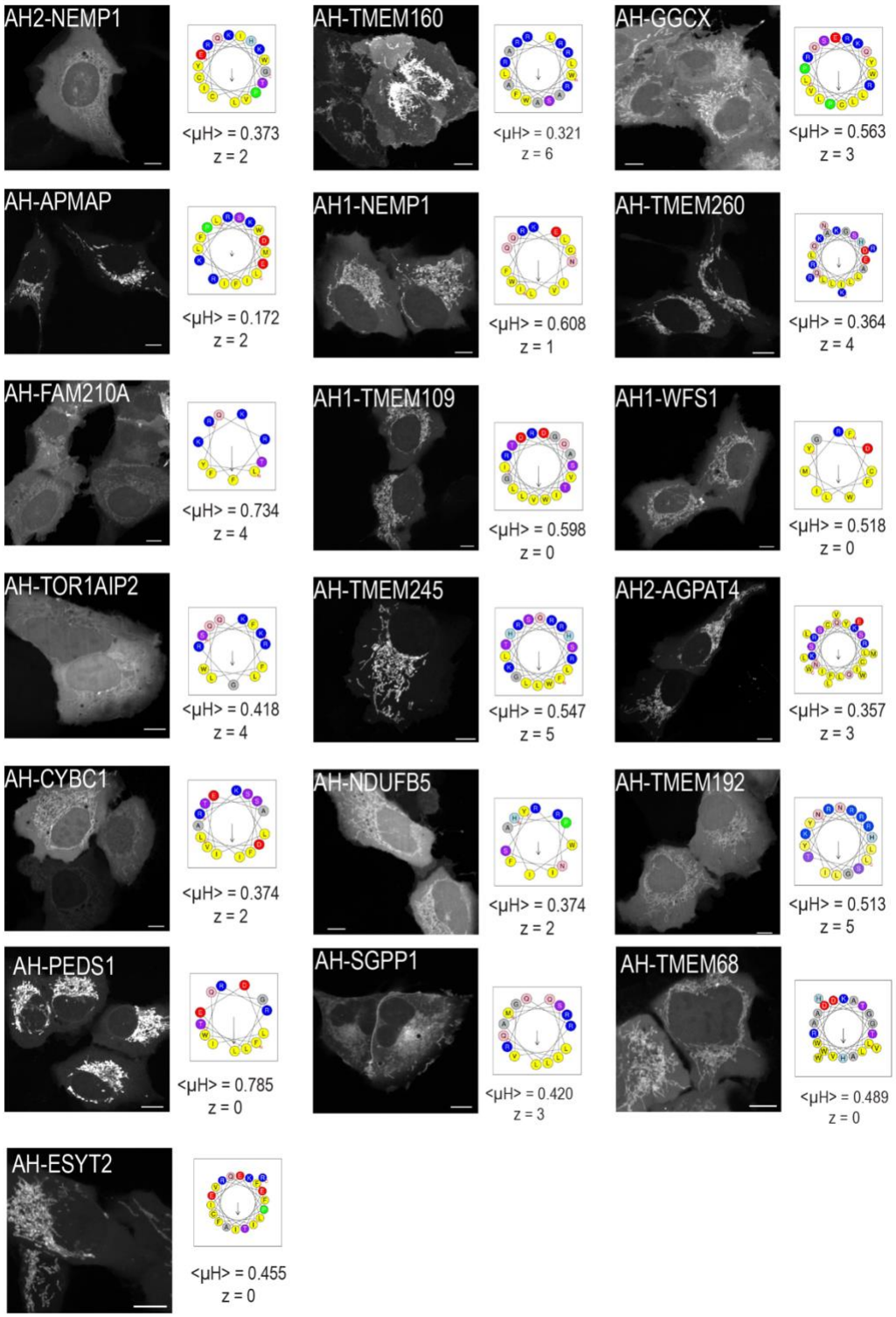

Fig. S5. Subcellular localization patterns of AH candidates tagged with mNG that displayed mitochondrial pattern.

Confocal images of live U2OS cells expressing the indicated AH-mNG constructs. Scale bars, 10 μm.

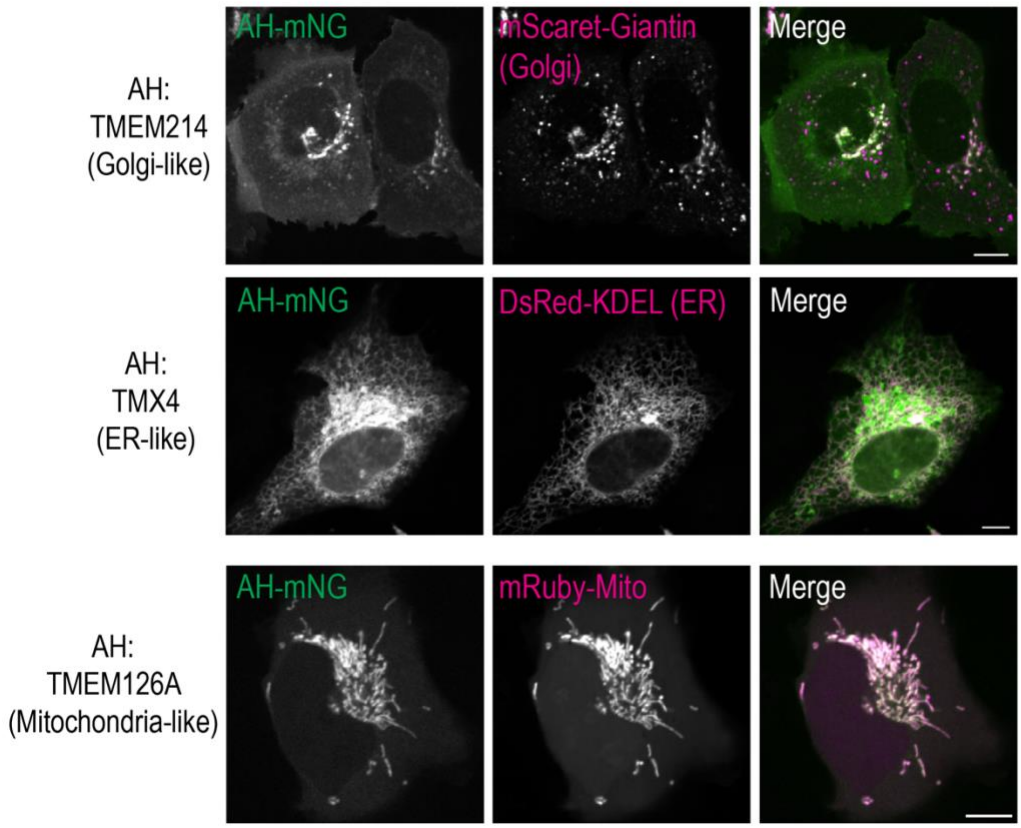

Fig. S6. Validation of the organelle type that AH-mNG constructs localized to.

Confocal images of live U2OS cells transiently expressing the indicated AH-mNG constructs with an organelle marker.

Scale bars, 10 μm.

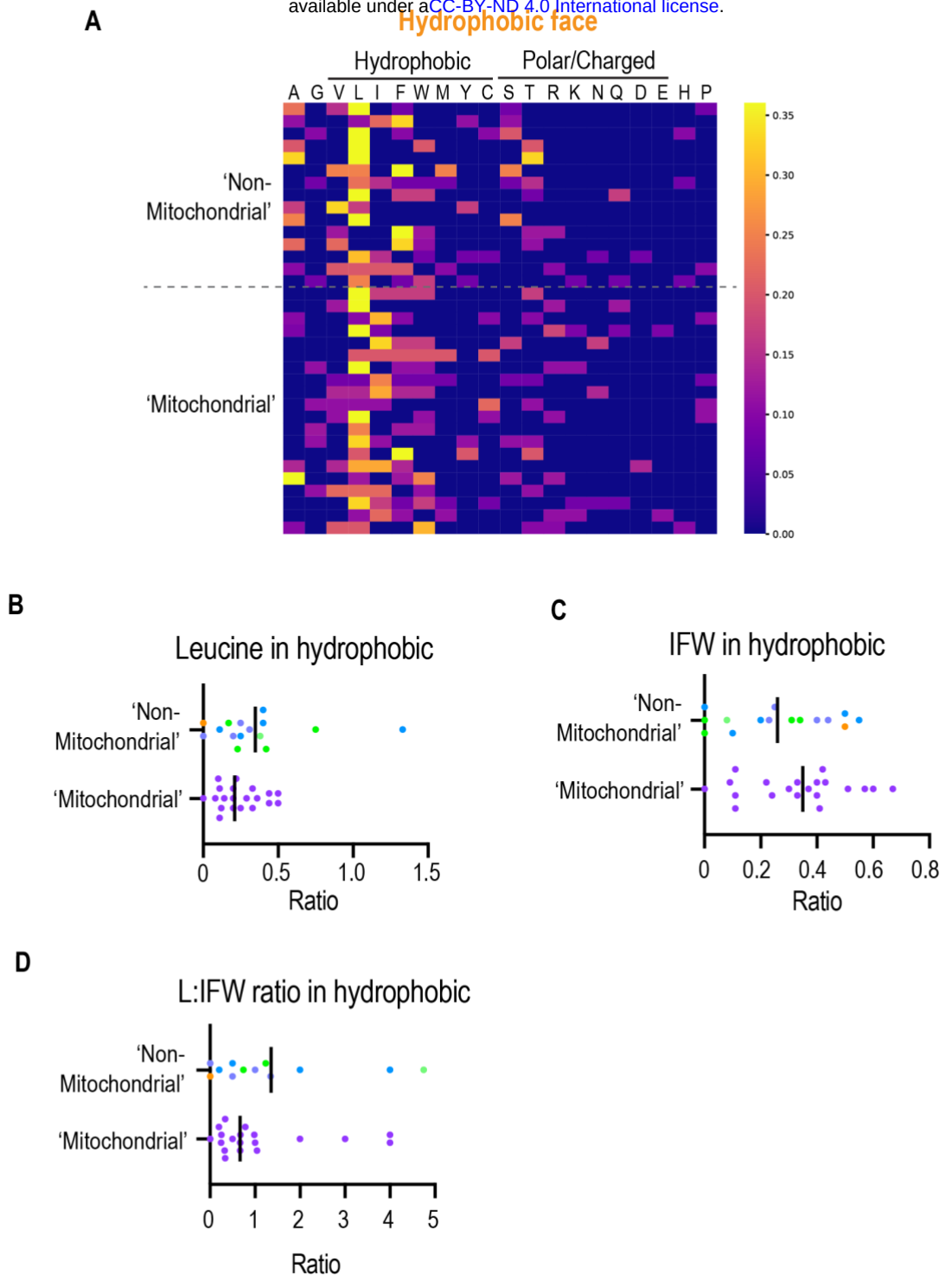

Fig. S7. Sequence codes in hydrophobic face that discriminate AHs with non-mitochondrial and mitochondria-like pattern.

(A) Heatmap of the amino acid compositions. Each raw represents an AH. (B-D) Scatter plots of the indicated matrices of AHs. Dots are color-coded by the subcellular localization patterns in Fig. 1B.

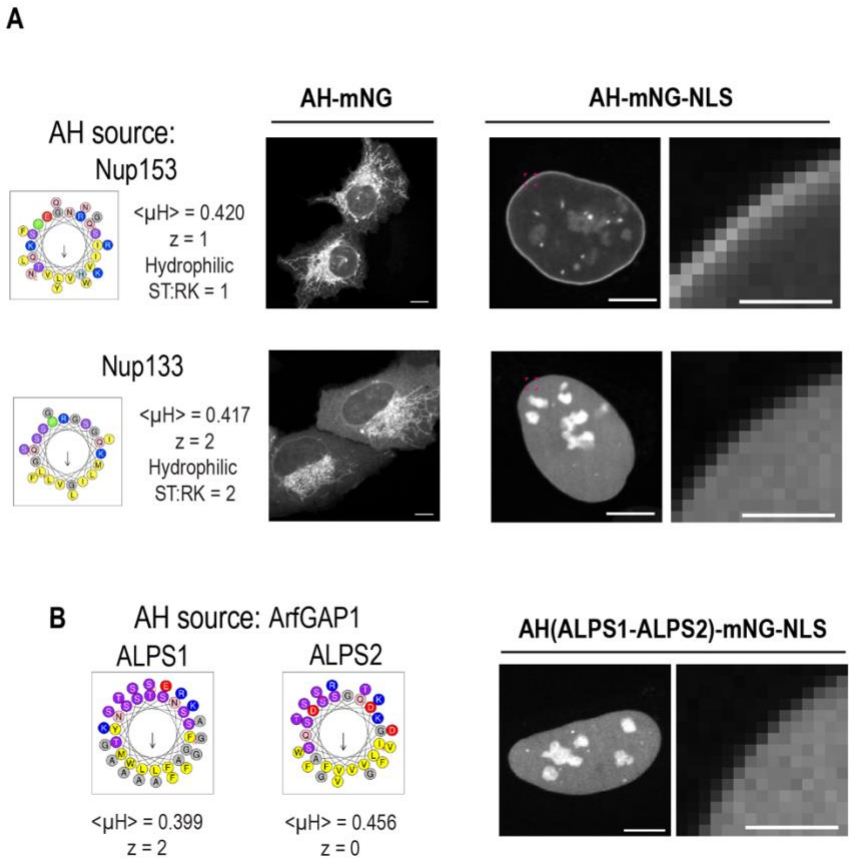

Fig. S8. Subcellular localization patterns and INM association of AHs from human Nup153, Nup133 and ArfGAP1.

Wheel projections of the indicated AHs and confocal images of live U2OS cells expressing the indicated constructs. Scale bars, 10 μm and 2 μm (zoom).

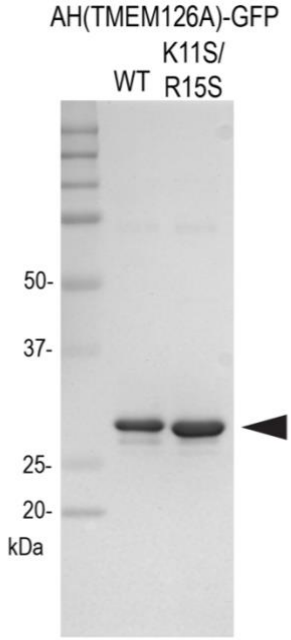

Fig. S9. Purification of AH-GFP.

Coomassie staining of the purified AH-GFP recombinant proteins.

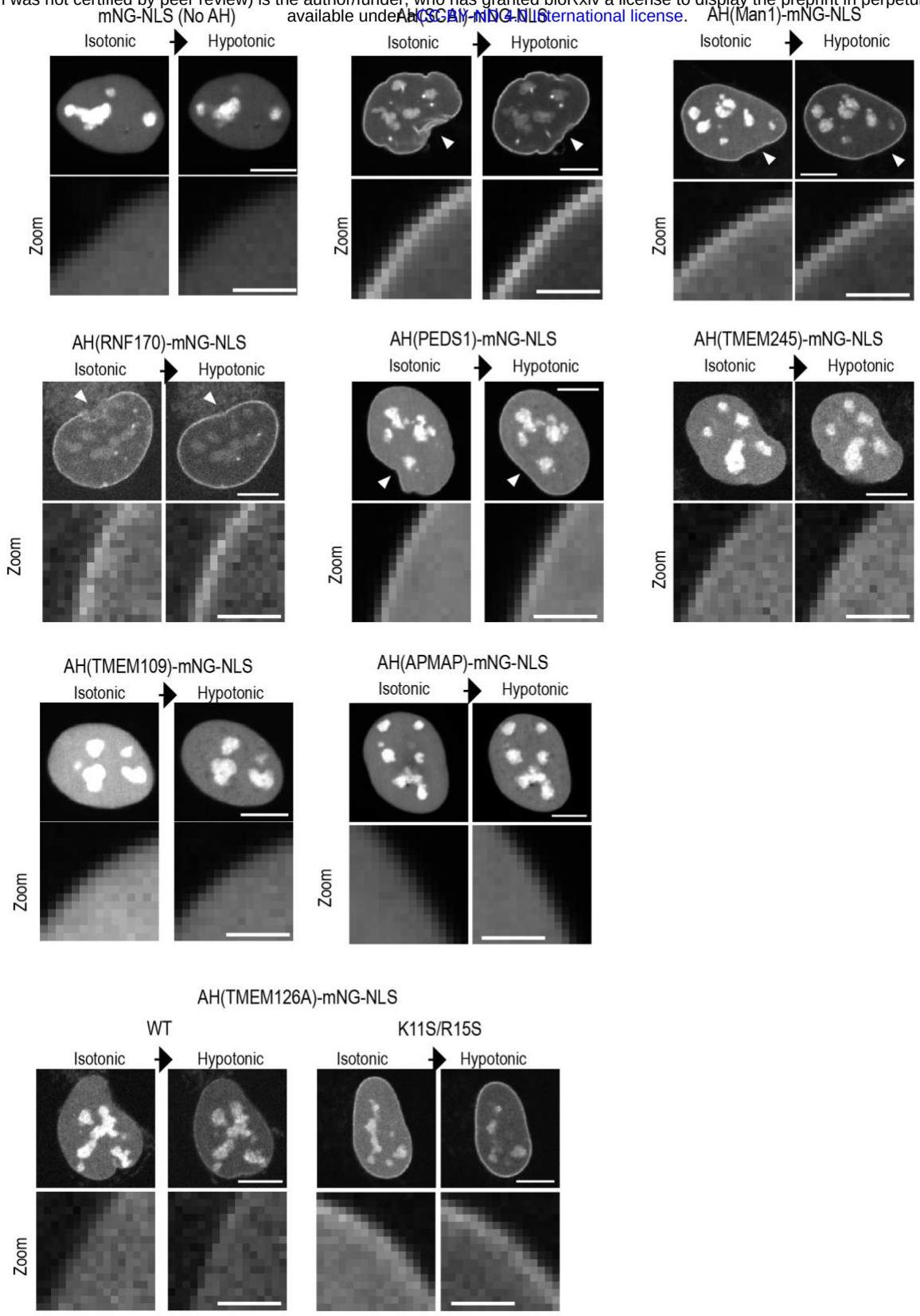

Fig. S10. A subset of NE protein AHs sensed membrane stretch of nuclear envelope.

Confocal images of live U2OS cells expressing the AH-mNG-NLS constructs before and after the hypotonic shock. Arrowheads indicate nuclear deformation upon hypotonic shock. Scale bars, 10 μm or 2 μm (zoom).

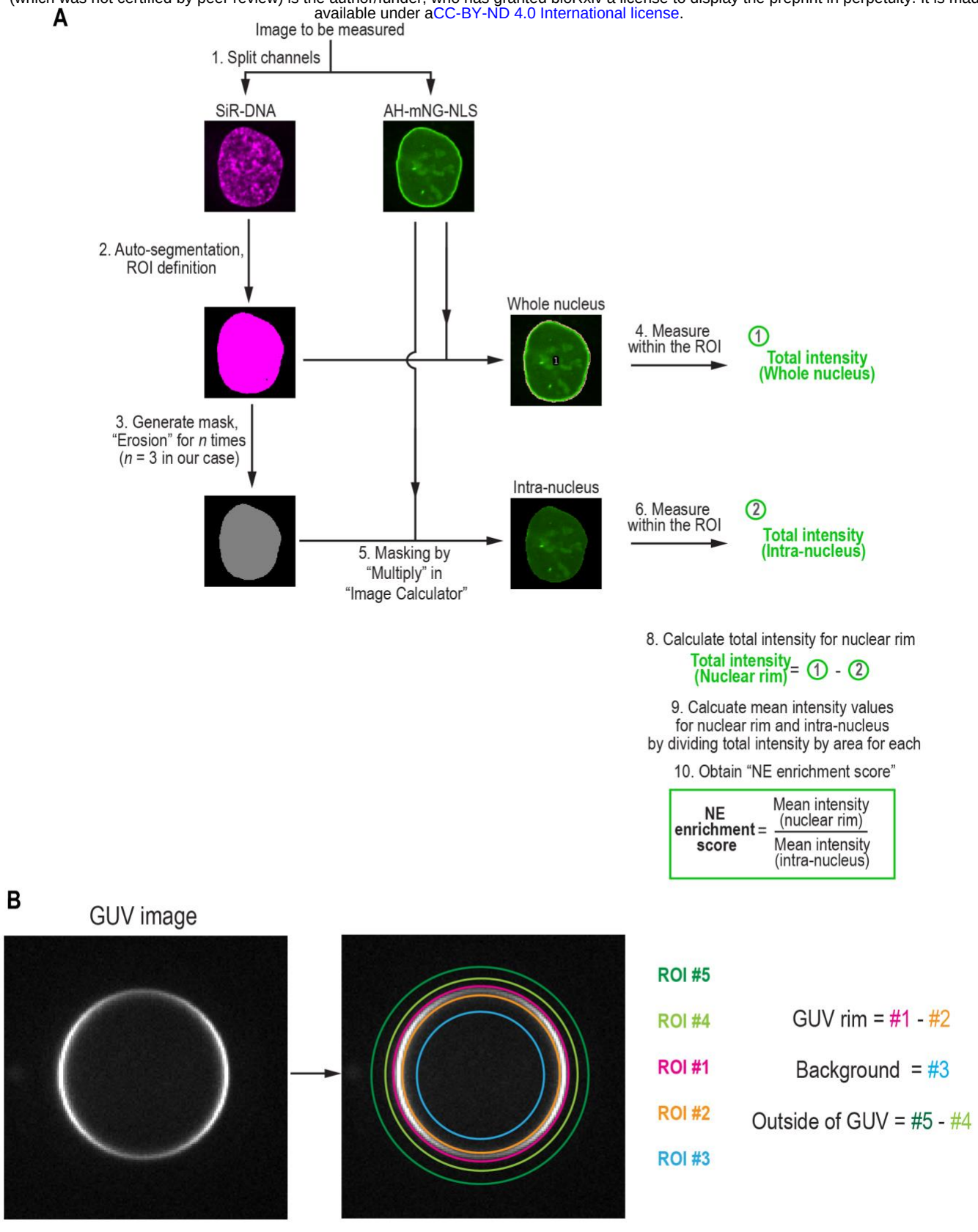

Fig. S11. Schematic of the image analysis.

(A) Workflow of the NE enrichment score quantification. (B) Illustration of the ROIs in the quantification of AH-GFP binding on GUV. See methods for more detail.